A structural basis for inhibition of the complement initiator protease C1r by Lyme disease spirochetes

Running Title: The molecular interface of BBK32/C1r

Ryan J. Garrigues[1], Alexandra D. Powell Pierce[2], Michal Hammel[3],

Jon T. Skare[2, *], and Brandon L. Garcia[1,*]

[1]Department of Microbiology and Immunology, Brody School of Medicine, East Carolina University, Greenville, North Carolina, United States of America

[2]Department of Microbial Pathogenesis and Immunology, College of Medicine, Texas A&M University, Bryan/College Station, Texas, United States of America

[3]Molecular Biophysics and Integrated Bioimaging, Lawrence Berkeley National Laboratory, Berkeley, CA, USA

Author Contributions

[*]These authors contributed equally to this work. Correspondence to Brandon L. Garcia (garciabr18@ecu.edu) and Jon T. Skare (jskare@tamu.edu).

J.T.S. and B.L.G. designed research; R.J.G., A.D.P., and M.H. performed research; R.J.G., A.D.P., M.H., J.T.S., and B.L.G. analyzed data; R.J.G., A.D.P., M.H., J.T.S, and B.L.G wrote the paper.

Abstract

Complement evasion is a hallmark of extracellular microbial pathogens such as *Borreliella burgdorferi*, the causative agent of Lyme disease. Lyme disease spirochetes express nearly a dozen outer surface lipoproteins that bind complement components and interfere with their native activities. Among these, BBK32 is unique in its selective inhibition of the classical pathway. BBK32 blocks activation of this pathway by selectively binding and inhibiting the C1r serine protease of first component of complement, C1. To understand the structural basis for BBK32-mediated C1r inhibition, we performed co-crystallography and size exclusion chromatography-coupled small angle x-ray scattering experiments, which revealed a molecular model of BBK32-C in complex with activated human C1r. Structure-guided site-directed mutagenesis was combined with surface plasmon resonance binding experiments and assays of complement function to validate the predicted molecular interface. The studies reported here, for the first time, provide a structural basis for classical pathway-specific inhibition by a human pathogen.

Introduction

The complement system consists of dozens of interacting soluble and surface-associated proteins that together form a primary arm of the innate immune system (*1–4*). Activation of complement on a microbial surface leads to opsonization, recruitment of professional phagocytes, and in many cases, direct cellular lysis. Complement activation involves a cascading series of proteolytic reactions catalyzed by specialized serine proteases that cleave circulating inert complement components into activated fragments. The cascade can be initiated in multiple ways, leading to a canonical grouping of complement activation into three pathways known as the classical, lectin, and alternative pathways. The classical pathway is initiated by a multiprotein

complex known as the first component of complement, C1 (*5–8*). C1 is composed of C1q, two molecules of C1r, and two molecules of C1s ($C1qr_2s_2$). C1q serves as the pattern recognition molecule of the classical pathway, binding to immune complexes and non-antibody ligands resulting in zymogen activation of the attached C1r and C1s proteases. The lectin pathway is similarly initiated by pattern recognition, whereby mannan-binding lectin (MBL), ficolins, collectin-10 or collectin-11 bind foreign carbohydrate structures and cause activation of the MBL-associated proteases (MASPs) (*9*, *10*). In contrast, the alternative pathway does not rely on pattern recognition but is instead continuously activated at a low level by a process known as 'tick-over' (*11*). All three initiating pathways converge at the cleavage of the central molecule of the cascade, complement component C3. C3 activation leads to formation of surface-bound enzyme complexes known as convertases that drive complement amplification and terminal pathway activation, ultimately resulting in the formation of the terminal pathway complete complex, C5b-9, also known as the membrane attack complex (MAC) (*1*, *2*).

Complement activation is a finely tuned process controlled by endogenous regulators of complement activity (RCAs) (*12*). RCAs are critical in preventing inappropriate complement activation on the surface of healthy host cells. Indeed, aberrant activation or overactivation of complement causes or exacerbates a wide range of human autoimmune, inflammatory, and neurodegenerative diseases (*13*, *14*). Microbes lack RCAs and thus many human pathogens have evolved sophisticated complement evasion systems to prevent complement-mediated attack (*15*). A prototypical example of a bacterial complement evasion system is found in *Borreliella* spirochetes (*16*, *17*). *Borreliella* gen. nov. encompasses the etiological agents of Lyme disease including the major genospecies *Borreliella burgdorferi, B. afzelii,* and *B. garinii* (*18*). The *Borreliella* complement evasion repertoire is overlapping and is categorized by two general

70 mechanisms (*16*, *17*). The first mechanism involves functional recruitment of host RCAs to the
71 spirochete, surface such as factor H (FH) (*19–28*). Among this group are the complement regulator
72 acquiring surface proteins (CRASPs) which include three distinct classes of FH-binding proteins
73 called CspA (CRASP-1), CspZ (CRASP-2), and three OspEF-related family paralogs known as
74 ErpP (CRASP-3), ErpC (CRASP-4), and ErpA (CRASP-5) (*19–28*). The second general
75 mechanism of complement evasion by outer surface *Borreliella* proteins involves a direct mode of
76 inhibition. Known inhibitors from this group include *B. bavariensis* BGA66 and BGA71 (*29*), a
77 FH-binding independent activity for CspA (*30*), and a protein of unknown molecular identity with
78 CD59-like activity that each interact with components of C5b-9 and prevent MAC formation (*31*).
79 In addition, two *Borreliella* outer surface lipoproteins are known to directly interfere with
80 upstream initiation steps of complement: OspC which binds to C4b and prevents classical/lectin
81 pathway proconvertase formation (*32*), and BBK32 which selectively blocks classical pathway
82 activation (*33*).

83 *B. burgdorferi* BBK32 is an outer surface-localized lipoprotein upregulated during the
84 vertebrate infection phase of the *B. burgdorferi* lifecycle (*34*). We have previously shown that a
85 *bbk32* mutant is significantly attenuated in murine models of infection due to defects in
86 dissemination and the inability of the borrelial cells to maintain a normal bacterial load (*35*, *36*).
87 BBK32 contains non-overlapping N-terminal binding sites for host glycosaminoglycans (GAGs)
88 and fibronectin and the contribution of BBK32 to Lyme disease pathogenesis is likely related to
89 its multifunctionality (*37*, *38*). Interactions by BBK32 with GAGs and fibronectin at the host
90 endothelium exhibit dragging and tethering, respectively, thereby promoting adherence during to
91 the shear force of blood flow, resulting in the hematogenous dissemination of *B. burgdorferi* via
92 extravasation (*39*, *40*). More recently, we identified a potent complement inhibitory activity for

93 the C-terminal domain of BBK32 (BBK32-C, hereafter) (*33*). BBK32-C binds directly to the C1
94 complex and blocks the earliest proteolytic events of the classical pathway of complement (*33*).
95 The classical pathway-selective inhibitory activity of BBK32 is currently unique among known
96 microbial complement evasion proteins.

97 We have previously shown that BBK32-C binds the human C1 complex by specifically
98 recognizing the C1r subcomponent with high-affinity (*33*). Recently we obtained a high-resolution
99 crystal structure of BBK32-C and mapped its binding site on human C1r to the serine protease
100 (SP) domain (*41*). Collectively, these studies showed that BBK32-C blocks C1r autoactivation,
101 as well as C1r-mediated cleavage of its partner protease in the C1 complex, C1s (*33*). However,
102 the structural basis and mechanism of action for BBK32-mediated C1r inhibition remains
103 unknown. To gain further insight into the nature of the BBK32/C1r protein-protein interaction, we
104 carried out a series of co-crystallography and size exclusion chromatography-coupled small angle
105 x-ray scattering (SEC-SAXS) experiments followed by a structure-guided mutagenesis strategy
106 involving biophysical, biochemical, and microbiological approaches. These investigations reveal
107 the structural basis for C1r inhibition by Lyme disease spirochetes, provide insight into BBK32's
108 C1r selectivity, and reveal a convergent inhibitory mechanism between a spirochete and a
109 hematophagous eukaryotic organism.

110

111 **Results**

112

113 **The Structure of BBK32-C in Complex with Human C1r.**

114 We have previously shown that BBK32-C interacts with high affinity with an autolytic C-
115 terminal region of human C1r corresponding to residues 300-705 (UNIPROT numbering) (*41*).
116 Co-crystals of BBK32-C in complex with this fragment of C1r produced crystal samples that
117 generally did not yield diffraction data beyond 10 Å limiting resolution. Ultimately, a single

118 sample was produced that diffracted to 4.1 Å. Unfortunately, this dataset was characterized by
119 significant data pathologies including severe anisotropy and low completeness. Despite this, a
120 reasonable final solution (PDB: 7MZT) could be obtained for a single copy of the BBK32-C/C1r
121 complex for which readily interpretable electron density maps were observed (**Fig. 1 A, S1 A-C**
122 and **Table S1**). A large protein-protein interface between BBK32-C and the SP domain of C1r,
123 totaling 1,340 $Å^2$ buried surface area (b.s.a.), was present in this structure (**Fig. 1 A, D, S1 A**).
124 However, underlying data quality issues prevented a complete modeling of the asymmetric unit in
125 this crystal (see *Materials and Methods* for a detailed description). This led to elevated R_{free}/R_{work}
126 values (36.9%/37.2%) outside of the normal range for high quality crystallographic solutions (i.e.
127 < 30% R_{work}). Despite extensive effort to overcome these issues, including co-crystallization trials
128 with a variety of SP-containing C1r constructs, ultimately an improved crystallographic model
129 could not be obtained. We thus turned to an orthogonal approach involving the study of the
130 BBK32-C in complex with recombinant C1r-CCP2-SP in solution by SEC-SAXS.

131 SEC-SAXS curves were obtained for recombinant BBK32-C (**Fig. S2 A, D**), a recombinant
132 autoactivated C1r domain truncation construct (hereafter, C1r-CCP2-SP) (**Fig. S2 B, E**), and an
133 equimolar mixture of BBK32-C and C1r-CCP2-SP (**Figs. S2C, S3**). Radius of gyration (R_g) values
134 of 21.3, 24.0, and 27.8 Å were calculated from the Guinier region of the scattering curves for
135 BBK32-C, C1r-CCP2-SP, and BBK32-C/C1r-CCP2-SP samples, respectively (**Table 1**, **Figs. S2**
136 **D, E, S3 insets**). SAXS and multi-angle light scattering (MALS) determined molecular weights
137 (i.e., MW_{SAXS} and MW_{MALS}) are consistent with BBK32-C and C1r-CCP2-SP behaving as
138 monomeric species in solution (**Table 1**). For the BBK32-C/C1r-CCP2-SP sample, MW_{SAXS} =
139 55.6 kDa (*42*) and MW_{MALS} = ~55-65 kDa were determined, which are close to the expected
140 molecular weight of a 1:1 complex ($MW_{sequence}$ = 54.6 kDa). Analysis of each scattering curve

141 using a pair-wise distribution function, P(r), is also consistent with complex formation as
142 evidenced by the shape of the overlaid P(r) profiles and increased maximum particle size (D_{max})
143 of the BBK32-C/C1r-CCP2-SP samples relative to BBK32-C or C1r-CCP2-SP alone (**Fig. 1B,**
144 **Table 1)**.

145 Next, we compared the solution state of each unbound protein to available high-resolution
146 crystal structures of BBK32-C (PDB: 6N1L (*41*)) and the activated form of C1r-CCP2-SP (PDB:
147 1MD8 (*43*)). First, MODELLER (*44*) as implemented in UCSF Chimera (*45*), was used to model
148 missing loops into each structure, and theoretical scattering profiles of each model were then
149 generated and compared against the raw scattering profiles using Fast X-ray Scattering (FoXS)
150 (*46*, *47*). Good agreement between theoretical and experimental SAXS curves were obtained for
151 BBK32-C (χ^2 = 2.08) and C1r-CCP2-SP (χ^2 = 1.06) atomistic models (**Fig. S2 D, E, Table 1**).
152 Collectively, analysis of the experimental SAXS curves shows that solution states of unbound
153 BBK32-C and activated C1r-CCP2-SP are in agreement with previously published crystal
154 structures and that BBK32-C/C1r-CCP2-SP forms a 1:1 stoichiometric complex in solution.

155 To better define the molecular interface formed between BBK32 and human C1r, we employed
156 a SAXS-restrained macromolecular computational docking approach using FoXSDock (*48*). This
157 method – which relies on the availability of high-resolution structures of the individual complex
158 components – involves initial docking using a geometric shape-matching algorithm, coarse SAXS
159 filtering of the resulting docking models, scoring of the interface energies, and scoring the fit of
160 the model's theoretical SAXS profiles to the raw SAXS profile of the BBK32-C/C1r-CCP2-SP
161 complex (*47*). BBK32-C and C1r-CCP2-SP were docked as a ligand-receptor pair and each model
162 was compared against the BBK32-C/C1r-CCP2-SP SAXS curve. The top four models (as judged
163 by Z scores (*48*)), each exhibited nearly identical protein-protein interfaces involving BBK32-C

164 contact residues originating from helix 1, 5 and the short loop connecting helix 1 and 2. Consistent
165 with our previous mapping study (*33*), all C1r interactions in these four models involve only
166 residues within the C1r SP domain. We then reconstructed a molecular envelope using DAMMIF
167 (*49*, *50*), which produced a distinctive chevron shape (**Figs. 1D,** gray envelope). Superimposition
168 of the top scoring FoxsDock model onto the shape envelope results in a close match, further
169 supporting the validity of the interface (**Fig. 1D**). Minimal molecular dynamics simulations using
170 BILBOMD (*51*) were performed on the best scoring model (χ^2 = 1.28) to eliminate potential
171 clashes between side chains at the interface, further improving the model's SAXS score (χ^2 =
172 1.24) (**Fig. 1D, Table 1**). A structural alignment of the co-crystal structure to the top three scored
173 SAXS-derived structures reveals a highly similar protein-protein interface, with the primary
174 differences being related to the orientation of the BBK32-C helical bundle that does not participate
175 in C1r interaction (**Fig. 1 C, E**). Furthermore, a model of 7MZT that lacks the C1r-CCP1 domain
176 fits closely to the experimental SAXS curve obtained for BBK32-C/C1r-CCP2-SP, as judged by
177 FoXS (χ^2 = 1.20) (**Fig. S3**).

178 **Analysis and Validation of the BBK32-C/C1r Structure**

179 Protein-protein interaction analysis was carried out using the SAXS-derived structure of
180 BBK32-C in complex with C1r-CCP2-SP using the programs PISA and CCP4 CONTACT (*52*,
181 *53*). The model predicts an interaction involving 28 contact residues on the BBK32-C side and 34
182 contact residues from human C1r, resulting in of 1,270 Å^2 b.s.a. (**Fig. 1E, 2A**). To validate the
183 predicted interface, we carried out structure-guided site-directed mutagenesis. A total of eleven
184 BBK32-C residues comprising > 50% of the total surface area buried by BBK32-C were changed
185 to alanine in single and/or double mutant forms (**Fig. 2A**, red). These mutants were then evaluated
186 for direct relative binding to C1r-CCP2-SP by surface plasmon resonance (SPR).

187 To evaluate BBK32 mutants on the same surface, we initially captured HIS-C1r-CCP2-SP
188 uniformly on an Ni-NTA sensorchip and binding of BBK32-C was monitored using a single-cycle
189 injection strategy (*54*) (**Fig. 2B**). Binding of BBK32-C to the HIS-C1r-CCP-2SP biosensor is
190 characterized by a long complex half-life (**Fig. 2B**, blue lines). However, this feature combined
191 with a small upward baseline drift of the reference-subtracted sensorgram, which was related to
192 the affinity-capture-based surface, resulted in poorly determined equilibrium dissociation K_D
193 values when fitted to a single-cycle kinetic model of binding. To overcome this limitation, and to
194 better match the expected physiological orientation of the interaction under study, we evaluated
195 C1r-CCP2-SP analyte injections over immobilized BBK32 sensorchips generated by amine-
196 coupling chemistry (**Fig. 2C**). Baseline drift was minimal using this covalently-coupled biosensor.
197 BBK32-C biosensors were created at two immobilization densities for better comparison to
198 individual site-directed mutant surface densities. The resulting low and high density sensorgrams
199 fit well to a 1:1 Langmuir kinetic binding model as judged by residual plots (**Fig. 2C** blue lines,
200 **Figs. S4**, **S5,** and **Table S2**). Consistent with our previous SPR binding measurements of BBK32-
201 C for C1, C1r, an autolytic fragment of C1r, and HIS-tagged recombinant domain truncations of
202 C1r (*33*, *41*), BBK32-C bound to activated C1r-CCP2-SP with high affinity, exhibiting an
203 equilibrium dissociation constant (K_D) of 0.45 nM (high density surface) and 0.78 nM for the low
204 density surface (**Fig. 2C, Table S2**).

205 Each BBK32 site-directed mutant was then evaluated by generating individual biosensors,
206 carrying out a C1r-CCP2-SP titration series, calculating an associated K_D, and comparing to the
207 BBK32-C biosensor that most closely matched wild-type surface density (**Fig. 2C, S4, S5**). Three
208 different double alanine mutants involving mutagenesis of small contiguous contact surfaces
209 resulted in a 653-fold (K327A-T331A), 127-fold (T242A-Y245A), and 615-fold (Y323A-E324A)

210 reduction in affinity for C1r-CCP2-SP, whereas a fourth such mutant retained an affinity similar
211 to wild-type (L236A-T239A) (**Figs. 2C, S4, S5, Table S2**). In the case of T242A-Y245A and
212 Y323A-E324A, single mutants retained wild-type-like affinity, indicating that the observed
213 affinity loss in the double mutants was due to a cumulative disruption of a larger contact surface
214 area (**Fig. 2C**). In contrast, a single K327A mutant resulted in a 153-fold loss in affinity, whereas
215 the paired T331A single mutant had near wild-type affinity (**Fig. 2C**). Additional mutagenesis was
216 directed at two arginine residues (R248 and R337). While a single R337A mutant exhibited wild-
217 type like affinity, mutation of R248 resulted in a 13-fold loss in affinity for C1r-CCP2-SP (**Fig.
218 2B, C, S4, S5**). Although they do not form a contiguous binding surface, a pairing of the two
219 strongest loss-of-affinity single mutants (i.e., R248A-K327A), produced a double mutant where
220 no detectable binding signal was observed (**Fig. 2B, C, S5**). In all cases, loss of affinity was driven
221 by increased dissociation rate constants (k_d) (**Table S2**). Similar qualitative results were obtained
222 for the single and double mutants of R248A and K327A as analytes over the HIS-C1r-CCP2-SP
223 biosensor (**Fig. 2B**), indicating that surface orientation and/or surface density did not greatly
224 influence the measurement of relative binding strength for these mutants. Taken together, these
225 data show that many BBK32 residues predicted to contact C1r-CCP2-SP in the SAXS structure
226 (**Fig. 2A**) exhibit a loss of affinity when mutated to alanine and that R248 and K327 are critical
227 hotspot residues for mediating C1r-CCP2-SP interaction.

228 **BBK32 Occludes Subsites Within the Active Site of C1r**

229 Having taken steps to validate the structural models, and in so doing, identifying key
230 interactions that mediate BBK32-C/C1r complex formation, we then analyzed the structure for
231 potential clues into the mechanism of C1r inhibitory action by BBK32. C1r is a modular serine
232 protease with a chymotrypsin-like SP domain (*55*). We noted that the BBK32 binding site on

233 human C1r is in close proximity to the C1r catalytic site (**Fig. 3A**). Although limited contacts are
234 made in the model with active site residues (28 $Å^2$ b.s.a.), much more extensive interactions are
235 made with the specificity pocket subsites S1 (176 $Å^2$ b.s.a.) and S1' (167 $Å^2$ b.s.a.) (**Fig. 3B**).
236 Residues involved in S1 (red) and S1' (blue) subsite interactions were mapped onto the BBK32-C
237 surface (**Fig. 3B**). These include three residues (T242, Y245, and R248) that were shown to have
238 loss of affinity effects when mutated to alanine (**Fig. 2**).

239 The steric occlusion of the S1 and S1' site by BBK32 in the model predicts that it would
240 also be capable of directly blocking the hydrolysis of small peptide C1r substrates, as well as the
241 larger natural C1r substrates, C1r and C1s proenzymes. Previously, we have shown that BBK32
242 blocks cleavage of proenzyme C1s by isolated C1r enzyme using an SDS-PAGE-based readout
243 (*33*). We adapted this assay to one that utilizes a colorimetric substrate specific for C1s enzyme
244 (i.e. Z-L-Lys thiobenzyl), and found that BBK32-C, but not R248A-K327A, could prevent
245 activation of proenzyme C1s by C1r enzyme. Similar results were obtained when C1r-CCP2-SP
246 cleavage of a colorimetric peptide substrate that requires only P2-P1-P1' access (i.e. Z-Gly-Arg-
247 thiobenzyl) was monitored (**Fig. 3C**). Furthermore, BBK32-C, but not R248A-K327A, prevented
248 cleavage of this substrate by spontaneously autoactivated full-length proenzyme C1r (**Fig. 3C**). To
249 further evaluate the interaction of BBK32-C with the proenzyme form of C1r, we produced two
250 forms of zymogen-stabilized C1r-CCP2-SP mutants. Both the scissile loop (i.e. R463Q) and
251 catalytic serine-based (S654A) zymogen forms of C1r-CCP2-SP bound similarly to BBK32-C,
252 and like autoactivated C1r-CCP2-SP, exhibited slow dissociation rates (**Fig. 3D**). Together, these
253 data show that BBK32 directly blocks both small and large C1r substrates from proteolytic
254 cleavage and that BBK32 recognizes both proenzyme and activated enzyme forms of C1r.

255 **R248 and K327 are Critical for BBK32-C Complement Inhibitory Activity**

256 Next we tested our panel of structure-based recombinant mutants for their ability to block
257 serum-based human complement activation in an ELISA assay that detects the classical pathway
258 activation product C4b. BBK32-C exhibited a half-maximal inhibitory concentration (IC_{50}) of 15
259 nM in this assay format (**Fig. 4A, Table S2**), consistent with our previously reported value of 5.6
260 nM (*33*). With the exception of E324A, which is discussed below, near wild-type IC_{50} values were
261 measured for all BBK32-C mutants that retained high affinity for C1r-CCP2-SP, although we
262 noted a modest reduction in inhibitory activity in the Y245A (~5-fold), N251A (~6-fold) and
263 Y323A (~2-fold) single mutants (**Fig. S6 and Table S2**). Importantly, in all cases where mutants
264 exhibited a strong loss of affinity for C1r-CCP2-SP, they were also greatly impaired in their ability
265 to block classical pathway activation. For example, the contiguous surface double mutants Y323A-
266 E324A and K327A-T331A failed to block complement at any concentration, while a ~240-fold
267 weaker IC_{50} value for T242A-Y245A was measured (**Fig. S6 and Table S2**). Likewise, the R248A
268 mutant was attenuated ~28-fold, and neither the K327A nor the R248A-K327A mutant blocked at
269 any of the concentrations tested (**Figs. 4A, and Table S2**).

270 Based on the SAXS-derived BBK32-C/C1r-CCP2-SP structure we were able to identify
271 several BBK32 residues that are important for its activity. In particular, substitution of R248 and
272 K327 to alanine in single mutants, or as a double mutant, results in a significant reduction of both
273 C1r-binding and inhibitory activity. To study these residues in a more physiological setting, we
274 produced site-directed BBK32 'knock-in' strains in the *B. burgdorferi* B314 genetic background
275 (**Fig. 4B**). *B. burgdorferi* B314 lacks linear plasmids that encode many of the outer surface proteins
276 associated with infection, including BBK32 (*56*, *57*). Previously we have shown that when wild-
277 type BBK32 is expressed heterologously on the surface of *B. burgdorferi* B314, it protects these
278 normally serum-sensitive spirochetes from human complement-mediated bacteriolysis (*33*, *41*).

279 Introduction of the R248A mutant into *B. burgdorferi* B314 resulted in a minimal reduction in
280 inhibitory activity relative to wild-type BBK32, while spirochetes expressing K327A were
281 significantly more sensitive to human serum. Spirochetes transformed with the *bbk32* R248A-
282 K327A allele lost all protective activity and were indistinguishable from the vector-only control
283 (**Fig. 4C**). These data confirmed that the R248 and K327 residues are critical for eliciting
284 complement inhibitory activity in the context of full-length BBK32 on the outer surface of *B.*
285 *burgdorferi*. Western immunoblots showed that full length BBK32 was produced equivalently in
286 all mutants tested, indicating that the enhanced sensitivity of the R248-K327A double mutant was
287 not the result of proteolytic instability (**Fig. 4B**).

288 **BBK32-C Targets Non-Conserved C1r Loops Outside of the Active Site**

289 We have previously shown that BBK32 is highly selective for C1r-binding relative to C1s
290 (*33*). To gain insight into this phenomenon, and with no comparable C1r inhibitors having been
291 reported, we instead compared the BBK32-C/C1r-CCP2-SP SAXS structure to that of a previously
292 published crystal structure of a protein inhibitor of both the classical and lectin complement
293 pathways, known as gigastasin (*58*). Gigastasin differs in selectivity from BBK32 as it blocks C1s,
294 MASP-1 and MASP-2, but is a relatively weak inhibitor of C1r (*58*). Interestingly, the
295 gigastasin/C1s protein-protein interface shares common features with the BBK32-C/C1r-CCP2-
296 SP SAXS structure presented here. Namely, both inhibitors form extensive interactions with the
297 S1 and S1' subsites of their respective target enzymes. Furthermore, BBK32 and gigastasin each
298 interact with three or more residues in the A and D loops, as well as loop 2 (**Fig. 5**). However,
299 BBK32 differs from gigastasin in that it makes extensive interactions with the B loop of C1r. This
300 loop contains an insertion sequence making it longer in C1r compared to most other complement
301 serine proteases, including C1s (**Fig. 5**). Interestingly, the B loop also is thought to block the

302 binding of the antistasin domain of gigastasin making it a determinant of inhibitor specificity (*43*,
303 *58*). Of the 16 residues that comprise the C1r B loop, 10 form contacts with BBK32-C and none
304 are identical at the homologous position in C1s (**Fig. 5**). Considering the entire interface, 25 of the
305 34 C1r contact residues predicted by the BBK32-C/C1r-CCP2-SP SAXS structure are non-
306 identical in C1s (**Fig. 5**). Most of these arise from surfaces involving the S1' site and four C1r
307 loops (i.e. A, B, D, E loops), suggesting these interactions may underlie the selectivity of BBK32
308 for C1r. Given the vastly different three-dimensional structures of BBK32 and gigastasin (**Fig. 5**),
309 it appears that a bloodborne prokaryote (*B. burgdorferi*) and a blood-feeding eukaryote
310 (*Haementeria ghilianii*) have evolved complement inhibitors with at least partially convergent
311 mechanisms of action, while also evolving differential target selectivity.

312 **Discussion**
313

314 In the absence of regulation, complement activation at the microbial surface leads to
315 deposition of C3b or C4b on the microbe surface, recognition by innate immune cells due to the
316 presence of immobilized C3b and C4b, recruitment of leukocytes by the anaphylatoxins C3a and
317 C5a, stimulation of the adaptive immune response by each of these fragments, and direct
318 bactericidal action by C5b-9 (i.e., MAC) (*1*, *2*). While intracellular pathogens may be protected by
319 complement within an intracellular niche, extracellular pathogens like *Borreliella* spirochetes face
320 a continuous threat from the complement systems of their hosts.

321 *Borreliella* first encounter complement during the bloodmeal of an infected *Ixodes* sp. tick.
322 Following transmission from their arthropod vector into the vertebrate host, spirochetes must
323 continue to protect themselves from complement during hematogenous dissemination, a challenge
324 that persists once they colonize distant tissues. To evade complement attack, Lyme disease
325 spirochetes express nearly a dozen different outer surface lipoproteins that directly interact with

326 complement proteins and modulate their native activities (*16*, *17*). While we have previously
327 shown that *B. burgdorferi bbk32* is required for optimal infectivity in naïve mice, it is likely that
328 C1r-specific inhibition by BBK32 also protects *B. burgdorferi* from targeted antibody-dependent
329 complement-mediated killing, a hallmark of the classical pathway. This contention is supported
330 by the persistent infection observed despite the presence of high titered antibody responses against
331 *B. burgdorferi* that can passively protect against borrelial infection and kill *B. burgdorferi in vitro*
332 in a complement-dependent manner (*59–61*).

333 In this study we aimed to determine the structural basis for the inhibition of C1r by *B.*
334 *burgdorferi* BBK32. A clear limitation of our study is the low resolution inherent to SAXS
335 experimental data. Importantly, the model presented here assumes limited conformational
336 rearrangement of BBK32-C and C1r-CCP2-SP relative to their unbound forms as previously
337 determined by crystallography. While analysis of the SAXS data for BBK32-C and C1r-CCP2-SP
338 suggests that each unbound protein adopts a similar structure in solution as they do in their
339 respective crystal structures (**Fig. S2**), we recognize that our approach would be unable to detect
340 larger scale conformational changes induced by BBK32-C/C1r-CCP2-SP complex formation. We
341 note that a highly similar interface is observed in the co-crystal structure presented here (**Fig. 1**),
342 although we acknowledge that the high R values and associated issues in the crystallographic data
343 quality are an additional limitation. Nonetheless, the validity of the SEC-SAXS-derived structure
344 is supported by its ability to successfully guide the identification of many BBK32 residues
345 important for driving both affinity and inhibitory activity (**Figs. 2-4**). Furthermore, the structure
346 provides a basis for an inhibitory mechanism that is consistent with the inhibitory activities and
347 selectivity of BBK32 (**Figs. 3-5**). Taken together, our data suggests that BBK32 inhibits human

348 C1r by simultaneously targeting its active site, as well as functionally critical, less conserved, non-
349 active site residues on loops of the C1r SP domain.

350 Like Lyme disease spirochetes, other bloodborne pathogens and blood feeding eukaryotes have
351 evolved complement evasion systems. For example, potent direct inhibitors of complement are
352 produced in the salivary glands of several species of ticks, including *Ixodes* sp. (*62–66*). Similarly,
353 blood-feeding insects like sandflies (*67*) and mosquitos (*68*), along with other human extracellular
354 pathogens such as *Staphylococcus aureus* (*15*, *69*, *70*), all produce a wide array of mechanistically
355 distinct protein inhibitors of complement. However, among known complement evasion
356 molecules, relatively few target the classical pathway with specificity (*70*), and to our knowledge
357 BBK32 remains the only reported selective inhibitor of C1r. Despite this, our study identifies a
358 surprising convergence of function between *B. burgdorferi* BBK32 and a complement protease
359 inhibitor of the classical and lectin pathways previously identified in the giant Amazonian leech
360 (i.e. gigastasin). However, gigastasin is related to a class of inhibitors known as antistasins (*71*),
361 that preferentially bind to the active form of their enzyme targets. This is in contrast to BBK32,
362 which recognizes both proenzyme and enzyme forms of C1r (**Figs. 2, 3**). While each inhibitor
363 functions, at least in part, by steric occlusion of the subsites upon enzyme-inhibitor complex
364 formation (*58*), it appears that differences in non-active site loops may drive selectivity of these
365 inhibitors (**Fig. 5**).

366 *Borreliella* spirochetes vary widely in their susceptibility to serum-based complement-
367 mediated bacteriolysis (*72*). While the categorizations are general and not without exceptions, *B.*
368 *burgdorferi* is typically considered serum-resistant whereas *B. garinii* is susceptible to killing by
369 human serum. The overall susceptibility of a spirochete to a particular host complement system is
370 related to the collective activities of the larger *Borreliella* complement evasion system (i.e.,

371 CRASPs, OspC, BBK32, etc.). However, insight into this host association phenomenon may be
372 gained from analysis of a single *Borreliella* complement inhibitor, in this case BBK32. While the
373 C1r-CCP2-SP binding affinity of nearly all mutants in our study correlated with the relative
374 inhibitory activity, a curious exception was BBK32-E324A. This mutant was reduced only two-
375 fold in affinity for C1r-CCP2-SP (**Fig. 2, S4**), but by several orders of magnitude in inhibitory
376 activity (**Fig. S6, Table S2**). BBK32-E324 is located next to K327 on the face of alpha helix 5 of
377 BBK32 and, like K327, is positioned across from the B loop of C1r in the model. In our previous
378 study we coincidentally probed the function of E324 while investigating the reduced complement
379 inhibitory activity of a BBK32 homologue from *B. garinii*, termed BGD19 (*41*). In that study, a
380 triple mutant chimeric recombinant protein termed BXK32-C was created to convert BBK32 to
381 BGD19 at three non-conserved residue positions (i.e., BBK32-E308K-Q319K-E324Q) (*41*). This
382 mutant shifted from BBK32-like to BGD19-like inhibitory activity, leading us to conclude that at
383 least one of these three surface-exposed residues was important for the complement inhibitory
384 activity of BBK32. Unlike R248 and K327, which drive human C1r affinity and are universally
385 conserved across publicly available *B. burgdorferi* genome sequences, position 324 is less
386 conserved (**Fig. S7**). While the underlying reasons for the disconnect between the binding and
387 inhibitory activities of these proteins remain unclear, we speculate that variation in position 324 in
388 naturally occurring BBK32 sequences may allow for optimal inhibition of C1r in other vertebrates
389 as the sequence of the C1r B loop is one of the least conserved features within vertebrate C1r.
390 Further studies, including high-resolution structural information involving synthetic or naturally
391 occurring BBK32 sequences such as *B. garinii* BGD19, along with mechanistic studies involving
392 non-human C1r or extensive C1r mutagenesis, will be needed to further test this possibility.

393 For the first time, this study provides a structural basis for classical pathway complement
394 evasion by a human pathogen. Among naturally occurring complement inhibitors, *B. burgdorferi*
395 BBK32 is unique in its ability to selectively target and inhibit the initiator protease of the classical
396 pathway, C1r, and, as such, the structure-function studies reported here provide new insight into
397 an evolutionarily optimized mechanism of action for C1r inhibition. This knowledge improves our
398 understanding of complement evasion by bacterial pathogens, increases our understanding of
399 naturally occurring complement inhibitors, and provides a potential basis for the development of
400 novel complement directed therapeutics that are classical pathway-specific.

401 **Materials and Methods**

402 *Strains, Plasmids constructed, and Oligonucleotides.*

403 All bacterial strains, plasmid constructs, and oligonucleotides used are listed in
404 supplemental **Table S3**. *B. burgdorferi* strain B314, with all recombinant plasmid constructs, was
405 grown in complete BSK-II media containing 300 µg/ml kanamycin as previously described (*41*).
406 *E. coli* cells were grown in LB media with kanamycin at 50 µg/ml.

407 Plasmid constructs for usage in *B. burgdorferi* strain B314 were constructed in a step-wise
408 manner. First, pCD100 was used as template to obtain the *bbk32*-R248A allele through use of the
409 oligonucleotides R248A mutant F and R248A mutant R that face in the opposite orientation and
410 contain the sequence to change codon 248. To facilitate this, GXL polymerase (Takara Bio) was
411 used with the following parameters: a 15 second denaturing step at 98°C, an annealing temperature
412 dependent on the lowest melting temperature of primers used for a specific reaction, and a 68°C
413 extension step for 1min/kb. The reaction was then digested with *Dpn*I (NEB), to digest methylated
414 parental DNA, and transformed into NEB5-alpha competent *E. coli*. The resulting plasmid was
415 designated pAP5. The *bbk32*-K327A encoding construct was obtained by synthesizing a 241 bp

416 fragment starting at nucleotide 861 and encompassing the remainder of *bbk32* and a 40 base pair
417 region of downstream sequence (IDT gBlocks). This fragment of *bbk32* contains native sequence
418 with the exception of the K327A codon. The K327A containing fragment and either pCD100 (for
419 pAP6 construction) or pAP5 (for pAP7 construction) were used as template with oligonucleotide
420 primers described in **Table S3** for PCR amplification. The resulting PCR products were assembled
421 using the NEBuilder HiFi DNA Assembly Cloning Kit as described in (*41*). The construct
422 encoding the *bbk32*-K327A allele was named pAP6. The final construct that encoded the *bbk32*-
423 R248A/K327A double mutant was designated pAP7. All plasmids were sequenced to ensure that
424 the desired mutations were obtained and that no additional mutations were introduced into *bbk32*.
425 Transformations of strain B314 with the aforementioned plasmid constructs were done as
426 described in (*73*, *74*).

427 For the production of all recombinant BBK32 proteins, DNA fragments for corresponding
428 site directed mutations in BBK32-C (residues 206-348, *B. burgdorferi* B31), for expression in *E.*
429 *coli*, were *E. coli* codon optimized and synthesized commercially by IDT Technologies gBlock
430 Gene Fragment service. The R337A mutant contained the C-terminal 6 residues in the full length
431 BBK32 sequence making it residues 206-354 (*33*). IDT gBlocks were designed with 5' BamHI,
432 3' NotI sites and stop codon, which then were subsequently cloned into pT7HMT as previously
433 described (*33*, *75*). Wild-type BBK32-C and C1r-CCP2-SP were expressed and purified form
434 previously generated constructs (*33*, *41*, *75*).

435 *Proteins*

436 Recombinant BBK32-C proteins were expressed and purified as previously described (*33*,
437 *41*), with the following modifications. After elution in Ni-NTA elution buffer (20 mM Tris (pH
438 8.0), 500 mM NaCl, 500 mM imidazole (pH 8.0)), proteins were exchanged into Ni-NTA-binding

439 buffer (20 mM Tris (pH 8.0), 500 mM NaCl, 10 mM Imidazole (pH 8.0)) using a Hi-Prep Desalting
440 26/10 column (GE Healthcare). To remove the HIS-myc affinity tag, proteins were incubated with
441 HIS tagged tobacco etch virus (TEV) protease and 5mM β-mercaptoethanol at room temperature
442 overnight. The digested proteins were then passed over a 5mL HisTrap-FF column and the flow-
443 through was collected for further purification by gel filtration chromatography using a HiLoad
444 Superdex 75 26/600 pg column (GE Healthcare). The monodisperse peak corresponding to
445 BBK32-C was pooled following analysis of chromatography fractions by SDS-PAGE and
446 exchanged into HBS (10mM HEPES (pH 7.3), 140mM NaCl). C1r-CCP2-SP, C1r-CCP2-SP
447 zymogen mutants, and His-C1r-CCP2-SP were purified according to methods as described
448 previously, with a final polishing step involving gel filtration chromatography on a HiLoad
449 Superdex 75 column (GE Healthcare) (*41*, *55*, *76*). His-tagged proteins were not subjected to HIS-
450 TEV cleavage. An autoproteolytic fragment of human C1r corresponding to residues 300-705
451 (UNIPROT: P00736) used in the co-crystallography experiment was obtained as previously
452 described (*41*). Full length complement proteins C1r proenzyme, C1r enzyme, and C1s proenzyme
453 were purchased from Complement Technology. In order to test for global changes in protein
454 folding that may be induced by site-directed mutagenesis, recombinant proteins were evaluated
455 for major changes in size by size exclusion chromatography (**Fig. S8**). Proteins were separated on
456 a HiLoad Superdex 200 Increase 10/300 column (GE Healthcare) and plotted against BioRad
457 Standards to determine size. Monodisperse peaks for all BBK32-C related samples exhibited a
458 ranging between 13.2 and 16.4 kDa.

459 *Statistical analysis*

460 Statistical analysis of assays was performed on GraphPad version 8. Calculations of IC_{50}
461 for classical pathway ELISA was determined with a normalized variable four-parameter fit.

462 Statistical significance for colorimetric enzyme assays were analyzed using a paired t-test.
463 Significance for *B. burgdorferi* serum sensitivity assays were analyzed using a two-way ANOVA
464 with a Šidák correction for multiple comparisons.
465
466 *Size exclusion chromatography-coupled Small Angle X-ray Scattering Data Collection*
467 Volumes of 60 µl samples containing either 8.0 mg mL^{-1} BBK32-C, 2.0 mg mL^{-1} C1r-
468 CCP2-SP, or 2.0 mg mL^{-1} BBK32-C/C1r-CCP2-SP 1:1 Complex were prepared in 10 mM HEPES
469 pH 7.3, 140 mM NaCl buffer. SEC-SAXS-MALS were collected at the ALS beamline 12.3.1
470 LBNL, Berkeley, California (*77*). X-ray wavelength was set at λ=1.127 Å and the sample-to-
471 detector distance was 2100 mm resulting in scattering vectors, q, ranging from 0.01 $Å^{-1}$ to 0.4 $Å^{-}$
472 ^{1}. The scattering vector is defined as $q = 4\pi\sin\theta/\lambda$, where 2θ is the scattering angle. All experiments
473 were performed at 20°C and data was processed as described (*78*). Briefly, a SAXS flow cell was
474 directly coupled with an online Agilent 1260 Infinity HPLC system using a Shodex KW802.5
475 column. The column was equilibrated with running buffer (10 mM HEPES (pH 7.3), 140 mM
476 NaCl) with a flow rate of 0.5 mL min^{-1}. 55 µL of each sample was run through the SEC and three
477 second X-ray exposures were collected continuously during a 30-minute elution. The SAXS
478 frames recorded prior to the protein elution peak were used to subtract all other frames. The
479 subtracted frames were investigated by radius of gyration (Rg) derived by the Guinier
480 approximation $I(q) = I(0) \exp(-q^2Rg2/3)$ with the limits $qRg<1.5$. The elution peak was mapped
481 by comparing integral of ratios to background and Rg relative to the recorded frame using the
482 program SCÅTTER. Uniform Rg values across an elution peak represent a homogenous assembly
483 (**Fig. S2**). Final merged SAXS profiles, derived by integrating multiple frames across the elution
484 peak, where used in PRIMUS (*79*) for further analysis including Guinier plot which determined

485 aggregation free state (**Figs. S2D-E, S3**). The program GNOM (*80*) was used to compute the pair
486 distribution function (P(r)) (**Fig. 1B**). The distance r where P(r) approaches zero intensity identifies
487 the maximal dimension of the macromolecule (D_{max}). P(r) functions were normalized to peak
488 maxima. Eluent was measured in line with a series of UV at 280 and 260 nm, multi-angle light
489 scattering (MALS), quasi-elastic light scattering (QELS), and refractometer detector. MALS
490 experiments were performed using an 18-angle DAWN HELEOS II light scattering detector
491 connected in tandem to an Optilab refractive index concentration detector (Wyatt Technology).
492 System normalization and calibration was performed with bovine serum albumin using a 45 µL
493 sample at 10 mg mL-1 in the same SEC running buffer and a dn/dc value of 0.19. The light
494 scattering experiments were used to perform analytical scale chromatographic separations for
495 MW_{MALS} determination of the principle peaks in the SEC analysis (**Fig. S2A-C**). UV, MALS, and
496 differential refractive index data was analyzed using Wyatt Astra 7 software to monitor the
497 homogeneity of the sample across the elution peak complementary to the above-mentioned SEC-
498 SAXS signal validation (**Fig. S2**).

499 *SAXS Solution Structure Modeling*

500 High resolution crystal structures for BBK32-C (PDB:6N1L) and C1r-CCP2-SP
501 (PDB:1MD8) were used for structural modeling (*41*, *43*). Missing residues, including the GSTGS
502 sequence cloning artifact, were added using COOT (*81*). In order to test multiple configurations
503 of residues added in this manner, structures were imported into UCSF-Chimera and the
504 MODELLER (*82*) tool was used to make five models. Each model was tested against SAXS data
505 in FoXS and the top scoring model was accepted. The BBK32-C/C1r-CCP2-SP complex was
506 determined by using FoXSDock (*47*) to perform rigid docking the highest overall score of the
507 almost 5000 models were accepted. Minimal molecular dynamics (MD) simulations using

508 BILBOMD (*51*) was performed on the best scoring model to eliminate potential clashes between
509 the residues side chains at the interface. The experimental SAXS profiles were then compared to
510 theoretical scattering curves generated from molecular models using the FOXS (*46*, *48*). Shape
511 envelope reconstruction for the BBK32-C/C1r-CCP2-SP sample was carried out using DAMMIF
512 as implemented in the ATSAS software suite (*49*, *83*). The final model was produced from the
513 average of ten models filtered for low occupancy using default values for DAMAVER/DAMFILT
514 (*50*).

515 *Crystallization, Structure Determination, Refinement and Analysis*

516 Purified BBK32-C and a purified autolytic fragment of human C1r (Complement
517 Technologies) were mixed at 5% molar excess BBK32-C and concentrated to 3.5 mg ml^{-1} in 10
518 mM HEPES (pH 7.3) 140 mM NaCl. Small plate-like crystals were obtained by vapor diffusion in
519 hanging drops at 20 °C by mixing 1 µl of protein solution with 1 µl of precipitant solution that had
520 been diluted into 3 µl of double deionized water. The precipitant solution contained 0.2 M sodium
521 formate and 27.5% (v/v) PEG 3,350. Crystals appeared in 2-5 days and were harvested and
522 cryoprotected in the precipitant solution supplemented with 5% (v/v) glycerol. Monochromatic X-
523 ray diffraction data were collected at 1.00 Å using beamline 22-ID of the Advanced Photon Source
524 (Argonne National Laboratory) using an Eiger 16M detector. While several samples were
525 harvested from this condition (and subsequent replications of this condition), only two samples
526 diffracted X-rays beyond ~10 Å and ultimately a single dataset was collected on one of these
527 crystals. Diffraction data were integrated, scaled, and reduced using the HKL2000 software suite
528 (*84*) and a high-resolution cut-off of 4.1 Å was chosen on the basis of I/σI and $CC_{1/2}$ (**Table 1**).
529 Consistent with the weak diffraction patterns observed, and difficulty in obtaining diffraction data
530 in certain crystal orientations, PHENIX XTRIAGE (*85*) analysis suggested several data

531 pathologies. This included severe anisotropy and low overall completeness. Additionally, strong
532 evidence of translational non-crystallographic symmetry was observed by Patterson map analysis.
533 Initial space group analysis suggested primitive tetragonal symmetry, however the final solution
534 was obtained in space group *P* 21 21 2 (**Table S1**). Molecular replacement was carried out with
535 PHASER in the Phenix software suite (*85*). Although translational non-crystallographic symmetry
536 was detected, the option to account for this automatically during MR was deselected after initial
537 failed solutions. An initial search was performed using a model of the monomeric activated form
538 of recombinant C1r-CCP1-CCP2-SP (PDB: 2QY0, (*86*)) where four C-terminal loop residues were
539 removed from Chain A. This search produced a solution in *P* 21 21 2 (LLG:248; TFZ: 18.9). This
540 solution was fixed, and a monomeric copy of BBK32-C was used for a subsequent search
541 producing a new solution (LLG: 424; TFZ: 17.8). Initial refinement of this solution using a single
542 round of individual B-factors was performed (R_{work} = 42.5% / R_{free} = 44.4%) producing readily
543 interpretable *2 F*o-*F*c density maps for both BBK32-C and C1r. Analysis of the asymmetric unit
544 suggested two copies of the complex were probable (one copy: 74.3% solvent content / Matthews
545 coeff.: 4.79 vs. two copies: 48.7% / 2.39). Additional exhaustive searches of various combinations
546 of the complex, complex subcomponents, or individual domains yielded highly scoring solutions,
547 however, presented unrealistic packing that could not be resolved by occupancy refinement.
548 Higher and lower symmetry space groups were explored with no improvement. While we
549 acknowledge other possibilities exist, our judgement is that two copies of the complex existed in
550 the crystal, but the second copy cannot be confidently placed due to the underlying poor data
551 quality and associated data pathologies of the crystal sample. Extensive efforts failed at producing
552 better quality crystal samples, leading us to turn to an alternative SAXS-based approach. However,
553 interpretable density of the single copy of the complex (**Fig. 1A, S1**) prompted us to carry forward

554 with refinement in the absence of the second suspected asymmetric unit copy. Analysis of the
555 contacts between BBK32-C and C1r in the obtained solution revealed three interfaces. Two of
556 these interfaces were sized consistent with crystallographic contacts (346 $Å^2$, and 344 $Å^2$) and one
557 large interface formed by a symmetry-mate of 1,108 $Å^2$, which was rearranged into the asymmetric
558 unit. Using this model, successive rounds of manual building using COOT (*81*) and iterative
559 individual B-factor refinement using PHENIX.REFINE resulted in the final model 36.7%/37.2%
560 (R_{work}/ R_{free}). A description of crystal cell constants, diffraction data quality, and properties of the
561 final model can be found in **Table S1**. Representations of protein structures and electron density
562 maps were generated in PyMol (www.pymol.org/).
563
564 *Surface Plasmon Resonance*
565 SPR experiments were performed on a Biacore T200 instrument at 25º C at a flowrate of
566 30 µL min^{-1} with a running buffer of HBS-T (10 mM HEPES (pH 7.3), 140 mM NaCl, 0.005%
567 Tween 20). Proteins were immobilized either on a NiD 200M Ni^{2+} chelator-modified sensorchips
568 or CMD 200 biosensor chips (Xantec Bioanalytics) using standard amine coupling as previously
569 described (*33*). For experiments involving immobilization of HIS-tagged species of C1r-CCP2-
570 SP, NiD 200M surfaces were conditioned for 5 min with 0.5 M Na-EDTA (pH 8.5), followed by
571 equilibration in HBS-T for 2 min. A solution of 5 mM nickel chloride was then injected for 2 min.
572 Next, HIS-tagged ligands were captured on individual flow cells at densities between 300-400 RU.
573 Single cycle injection curves were performed at five concentrations of BBK32-C or BBK32-C
574 site-directed mutants (1, 3.2, 10, 32, 500 nM). For experiments using amine coupling,
575 immobilization densities for each protein used in the study are presented in **Table S2**. Single cycle
576 injection curves were performed with a five concentration five-fold injection series of (0-500 nM)

577 C1r-CCP2-SP with 2 min association and a final dissociation time of 30 min. BBK32-C was
578 immobilized under two immobilization densities on adjacent flow cells on the same chip: BBK32-
579 $C_{High\ Density}$ (2011.4 RU) and BBK32-$C_{Low\ Density}$ (604.7 RU). Subsequent regeneration was
580 performed by three 30 s injections of a regeneration solution (0.1 M glycine (pH 2.2), 2.5 M NaCl).
581 Kinetic analysis was performed on each injection series using a 1:1 (Langmuir) binding model was
582 applied using Biacore T200 Evaluation Software (GE Healthcare). Equilibrium dissociation
583 constants (K_D) were determined from resulting fits and are shown as mean K_D. Quality of fits were
584 assessed by inspection of residual plots (**Fig. S4 .S5**).

585 *Classical pathway inhibitory assay*

586 Classical pathway inhibition was determined using an ELISA-based assay as previously
587 described (*33*, *41*, *87*). Briefly, high-binding 96 well plates (Grenier Bio-One) were coated with
588 human IgM (MP Biomedical) and activation of classical pathway was monitored using 2% normal
589 human serum (NHS; Innovative Research) and C4b detection was determined by monoclonal
590 antibody (Santa Cruz Biotechnology). Dose-dependent inhibition was performed using a 12-point,
591 two-fold dilution series of BBK32-C and mutants ranging from 1.1 to 2200 nM. Each assay was
592 performed at least in duplicate and normalized to in-column positive (no inhibitor) and negative
593 (no serum) controls.

594 *Serum complement sensitivity assay*

595 *B. burgdorferi* strain B314 were grown at 32°C in 1% CO_2 to early- to mid-log phase and
596 diluted in complete BSK-II media to a concentration of $1x10^6$ cell/ml. *B. burgdorferi* cells were
597 incubated in normal human serum (NHS; Complement Technology) at a final concentration of
598 15%. All strains were tested in duplicate independently four times. Samples were incubated at
599 37°C with gentle agitation for 1.5 hours with viability assessed by dark field microscopy.

600 Sensitivity was assessed by lack of motility, overt membrane damage, and/or cell lysis. The data
601 is represented as the average of all fields counted for biological replicates (40 minimum) in each
602 of the four independent assays.

603 *Immunoblots*

604 Western immunoblots were conducted to detect BBK32 from the parent and mutant
605 constructs produced in *B. burgdorferi* strain B314. Protein lysates were resolved by SDS-12.5%
606 PAGE and transferred to PVDF membranes. Membranes were incubated with either a monoclonal
607 antibody to BBK32 (diluted at 1:20,000) or *B. burgdorferi* strain B31 FlaB (Affinity BioReagents;
608 diluted at 1:10,000), washed, and then incubated with a 1:10,000 dilution of Goat anti-mouse IgG-
609 HRP (Thermo Fisher). The blots were processed to visualize the antigens as previously described
610 (*41*)

611 *C1s proenzyme activation assay*

612 Inhibition of C1r enzyme mediated activation of C1s proenzyme was assessed by a
613 colorimetric peptide cleavage assay. 2.2 µM BBK32-C or R248A-K327A was incubated with 25
614 nM C1r enzyme, 100 µM DTNB (5,5'-Dithiobis-(2-Nitrobenzoic Acid), Ellman's Reagent), and
615 C1s specific active site analog 100 µM Z-L-Lys-thiobenzyl (MP Biomedical). Lastly 3.13 nM
616 proenzyme C1s was added in HBS-T buffer (10 mM HEPES (pH7.3), 140 mM NaCl, .005%
617 Tween 20). Absorbance was monitored at 405 nm at 37º C on a Versamax plate reader for 1 hr in
618 triplicate. Data were in column normalized to no inhibitor and no C1s proenzyme controls.

619 *C1r peptide cleavage enzyme assays*

620 C1r-CCP2-SP or C1r proenzyme by BBK32-C or R248A-K327A, a colorimetric peptide
621 cleavage assay was employed (*55*). Single dose inhibition of 25 nM C1r-CCP2-SP or 25 nM C1r
622 proenzyme with 2.2 µM BBK32-C or R248A-K327A was performed in the presence of 300 µM

623 Z-Gly-Arg-thiobenzyl (MP Biomedical). Esterolytic cleavage was assayed by 100 µM DTNB
624 (5,5'-Dithiobis-(2-Nitrobenzoic Acid), Ellman's Reagent) in HBS-T buffer (10 mM HEPES
625 (pH7.3), 140 mM NaCl, .005% Tween 20). Absorbance was monitored at 405 nm at 25º C on a
626 Versamax plate reader for 1 hr in triplicate. Data were in column normalized to no inhibitor and
627 no C1r-CCP2-SP controls, with 100% cleavage defined as the amount of Z-Gly-Arg-thiobenzyl
628 cleaved by C1r-CCP2-SP in 1 hr at 25º C. Experimentation was performed in triplicate.

629 **Data Availability**

630 SAXS data and models are deposited in the Small Angle Scattering Biological Data Bank
631 (www.sasdb.org) with accession codes SASDKX7 (BBK32-C/C1r-CCP2-SP), SASDKV7 (C1r-
632 CCP2-SP), and SASDKW7 (BBK32-C). The co-crystal structure of BBK32-C/C1r$_{300-705}$ was
633 deposited into the Protein Data Bank, Research Collaboratory for Structure Bioinformatics,
634 Rutgers University (www.rcsb.org/) under the PDB code 7MZT.

635 **Acknowledgments**

636 SAXS data was collected at SIBYLS which is supported by the DOE-BER IDAT DE-
637 AC02-05CH11231 and NIGMS ALS-ENABLE (P30 GM124169 and S10OD018483). X-ray
638 diffraction data were collected at Southeast Regional Collaborative Access Team 22-ID beamline
639 at the Advanced Photon Source, Argonne National Laboratory. Supporting institutions may be
640 found at www.ser-cat.org/members.html. Use of the Advanced Photon Source was supported by
641 the US Department of Energy, Office of Science, Office of Basic Energy Sciences, under Contract
642 W-31-109-Eng-38. We thank Dr. Brian Geisbrecht (Kansas State University) for helpful
643 discussion related to this work. This study was supported by Public Health Service Grants
644 AI133367 and AI146930 (to JTS and BLG).

645

646 **Figures and Tables**

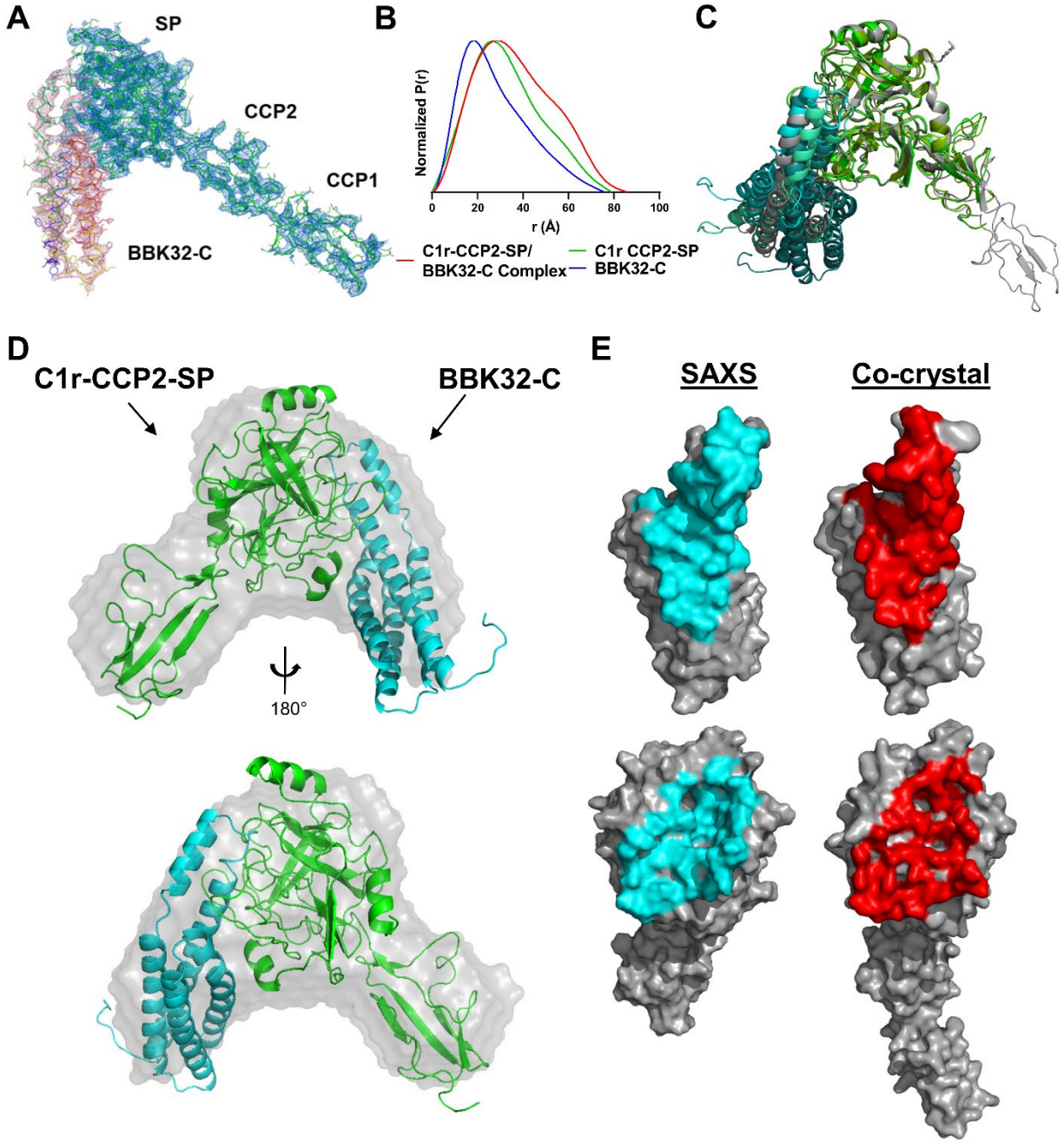

647

648 **Figure 1. Structures of BBK32-C in complex with human C1r fragments.**

649 **A)** The co-crystal structure of BBK32-C in complex with an autolytic fragment of C1r (residues

650 300-705) at 4.1Å (PDB: 7MZT) is shown with 2*Fo-Fc* density contoured at 1.2 σ for the BBK32-

651 C polypeptide (Chain I; pink mesh) and C1r (Chains A, B; blue mesh). **B)** Normalized pair
652 distribution curves (P(r)) of C1r-CCP2-SP/BBK32-C complex (red), C1r-CCP2-SP (green), and
653 BBK32-C (blue) derived from SEC-SAXS experiments. **C)** An overlay of the top three BBK32-
654 C/C1r-CCP2-SP SAXS models obtained from FoXS Dock as judged by χ^2 where C1r-CCP2-SP
655 are colored in shades of green and BBK32-C in shades of blue. PDB: 7MZT was aligned to the
656 C1r SP domain of the SAXS structures (grey). The protein-protein interface in each structure is
657 similar with the largest differences being attributed to the orientation of the helical bundle that
658 does not participate in the interface. **D)** *Ab initio* SAXS envelope (gray) aligned with SAXS
659 solution structure from FoXSDock, refined with BILBOMD. **E)** Contact residues as judged by the
660 EMBL PDBePISA server for the BBK32-C/C1r-CCP2-SP SAXS structure (left, cyan) and the
661 BBK32/C1r co-crystal structure (right, red).

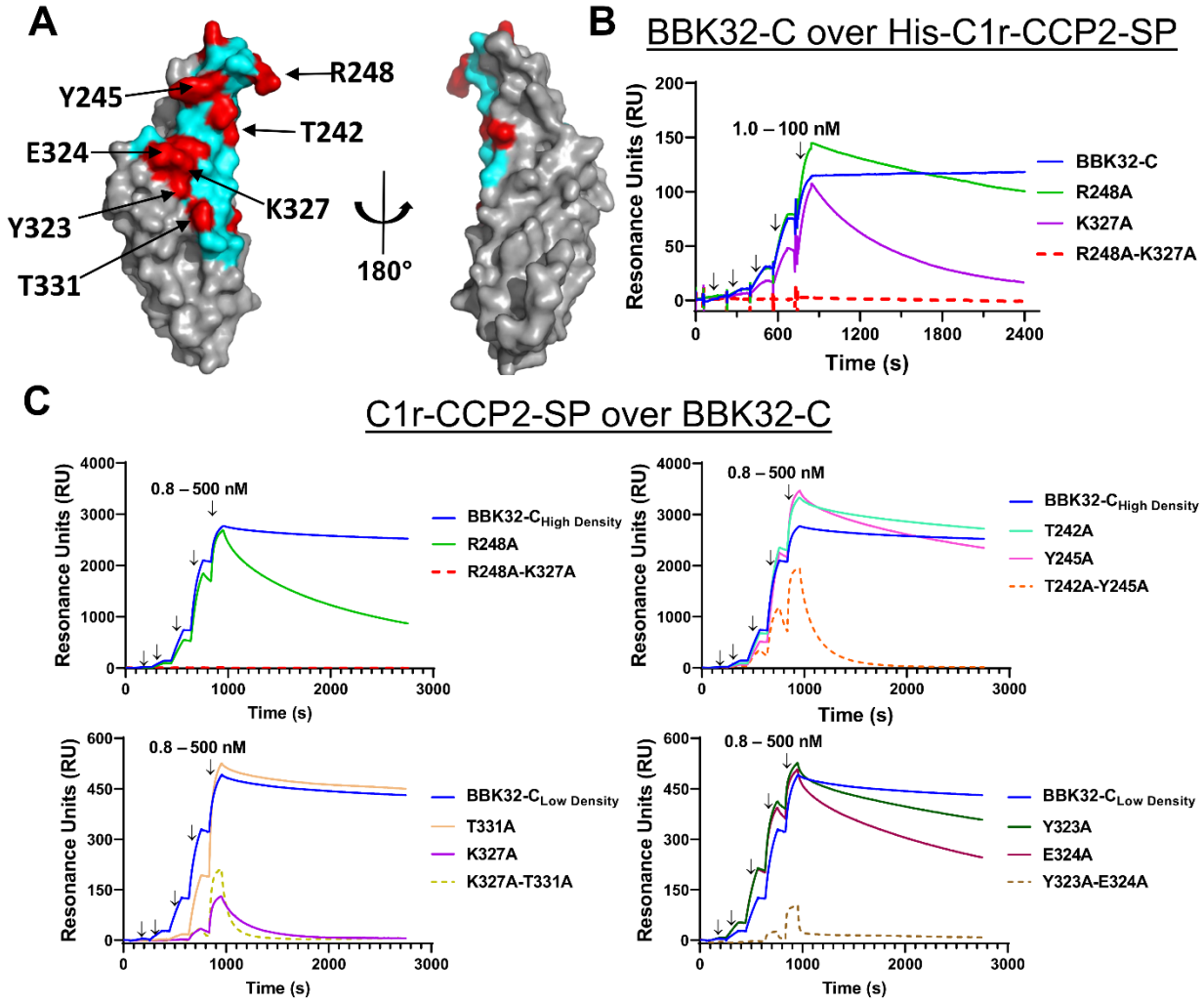

Figure 2. SPR binding assays with structure-guided site-directed BBK32 mutants. A) Surface representation of BBK32-C with non-contact surface areas (gray) and BBK32-C/C1r-CCP2-SP contact area (cyan). Residues mutated for this study (red) are indicated in **Table S2**. Site-directed mutants used in **Fig. 2B-C** are denoted with arrows. **B)** SPR experiments were performed by capturing His-C1r-CCP2-SP on a Ni-NTA sensor chip. BBK32-C and selected site-directed mutants were injected over the His-C1r-CCP2-SP surface in a concentration series (1.0, 3.2, 10.0, 31.6, 100 nM). Injection phases are denoted with arrows. **C)** SPR experiments were performed in the reverse orientation compared to panel **B** by immobilizing each BBK32 protein to sensor chips

using amine coupling chemistry. A fivefold concentration series of C1r-CCP2-SP (0.8, 4.0, 20.0, 100, 500 nM) was sequentially injected over each immobilized BBK32-C mutant. Arrows indicate injection phases of each C1r-CCP2-SP concentration. Representative sensorgrams are shown with ligands of similar immobilization density grouped with either high immobilization density BBK32-C (i.e., BBK32-$C_{\text{High Density}}$) or low immobilization density BBK32-C (i.e., BBK32-$C_{\text{Low Density}}$). BBK32-C curves are reproduced in each respective panel for comparison. SPR experiments were performed in duplicate. Dissociation constants (K_D) were calculated by kinetic fits with a 1:1 Langmuir model (**Fig. S4**, **S5, Table S2)**. Additional site-directed mutants analyzed by SPR and are shown in **Fig. S5**.

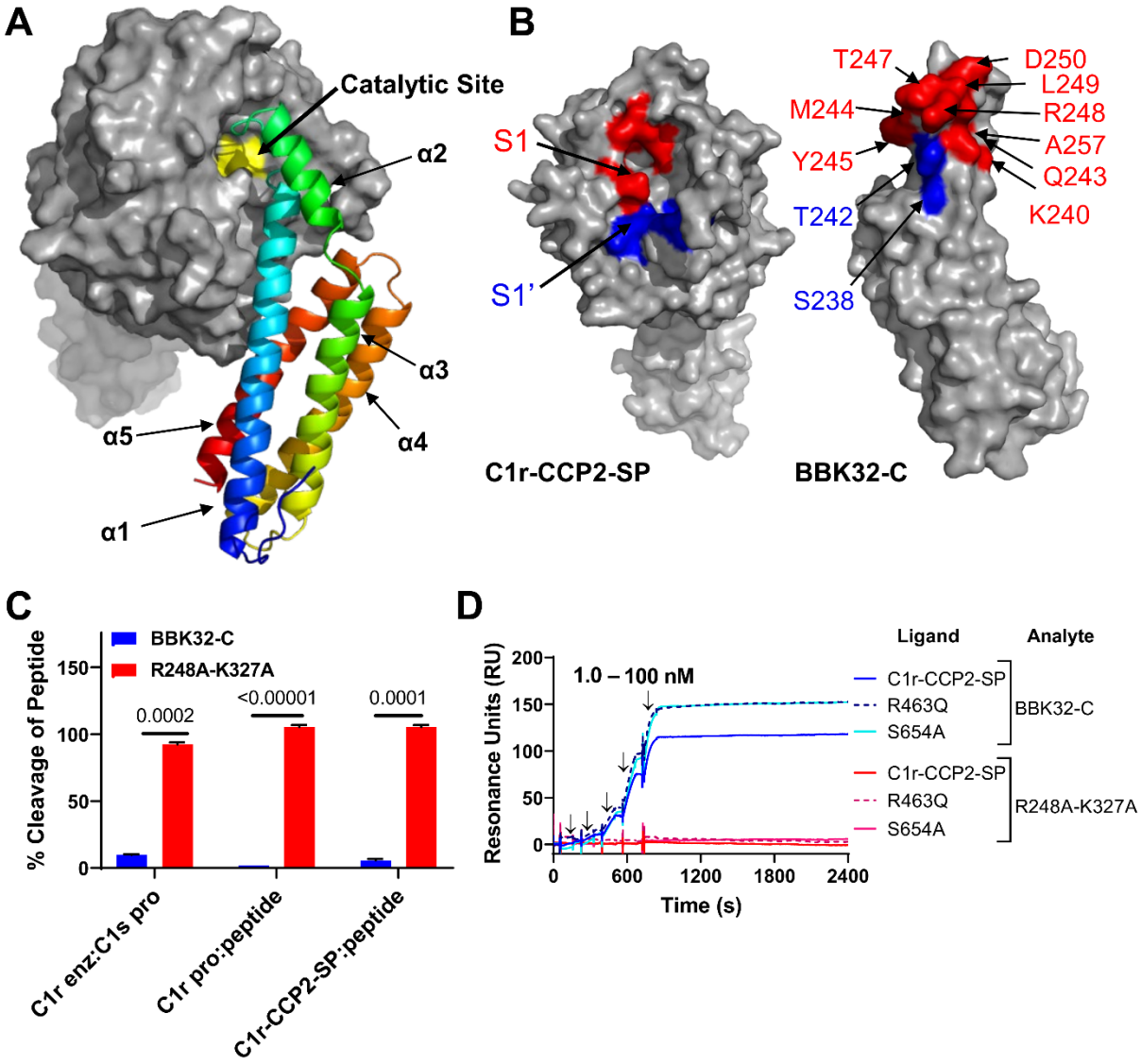

681

682 **Figure 3. BBK32-C occludes the S1 and S1' subsites on C1r. A-B)** C1r-CCP2-SP shown with
683 the catalytic site (yellow), substrate specificity subsites S1 (red) and S1' (blue) as determined by
684 Budayova and colleagues (*43*) using nomenclature provided by Schechter and Berger (*88*).
685 BBK32-C shown with residues that contact the C1r S1 site (red) and S1' site (blue). **C)** The ability
686 of BBK32-C or BBK32-R248A-K327A to directly inhibit cleavage of a small peptide or a natural
687 substrate was evaluated by colorimetric substrate-based enzyme assays. BBK32-C significantly
688 blocked C1r enzyme cleavage of C1s proenzyme, autocatalysis of C1r proenzyme and C1r-CCP2-

689 SP enzyme. All experiments were performed in triplicate and normalized to positive (no inhibitor)
690 and negative (no enzyme) controls. Statistical significance was evaluated using paired t-tests with
691 p-values noted above each experiment. **D)** To evaluate BBK32-C binding to zymogen-stabilized
692 forms of C1r-CCP2-SP, SPR experiments were performed by capturing His-C1r-CCP2-SP, His-
693 C1r-CCP2-SP-R463Q (R463Q), or His-C1r-CCP2-SP-S654A (S654A) on a Ni-NTA sensor chip.
694 BBK32-C was sequentially injected over each surface in a concentration series (1.0, 3.2, 10.0,
695 31.6, 100 nM). BBK32-C sensorgrams are reproduced from **Fig. 2B** for comparison. Arrows
696 indicate injection phases of each C1r-CCP2-SP concentration.

697

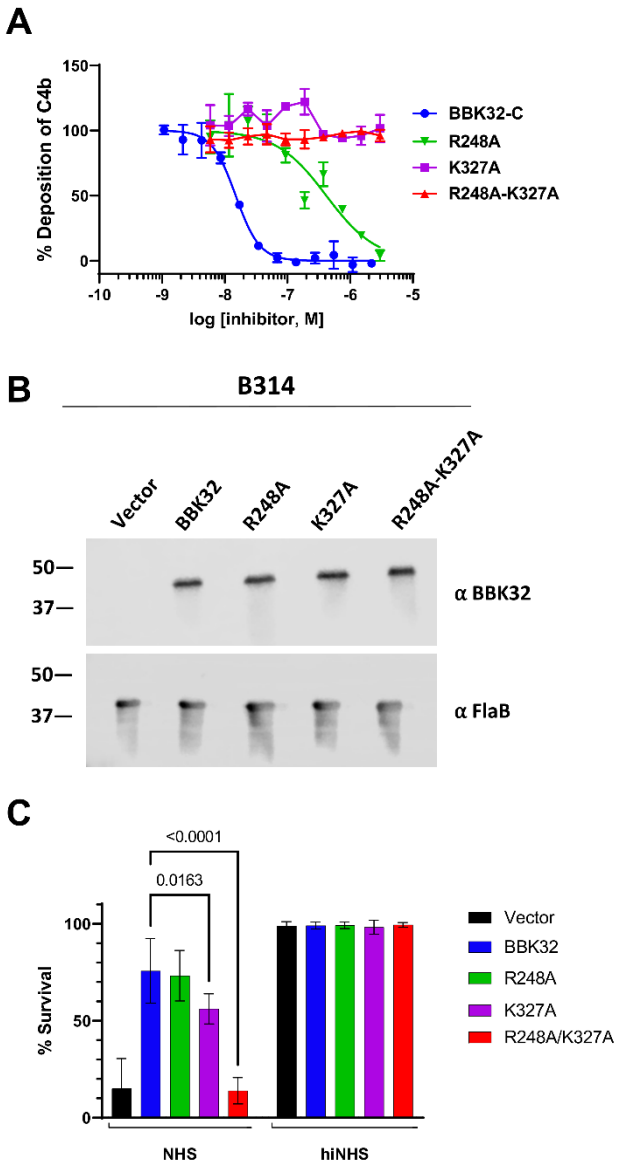

Figure 4. BBK32 R248 and K327 are critical for complement inhibitory activity of BBK32. A) ELISA-based complement activation assays were performed to determine the ability of BBK32-C mutants to inhibit the classical pathway of complement *in vitro*. A two-fold concentration series of each BBK32-C mutant was used and performed in duplicate. Inhibitory data for additional site-directed mutants are presented in **Figure S6**. IC_{50} values and 95% confidence intervals associated with a normalized four-parameter dose-inhibition fitting procedure are shown in **Table S2**. **B)** Western blots of lysates from *B. burgdorferi* strains B314 containing

718 distinct *bbk32* alleles were probed with monoclonal antibodies to BBK32 (α-BBK32) or FlaB (a-
719 FlaB), the latter as a loading control. Vector refers to the plasmid only backbone sample
720 (B314/pBBE22*luc*), BBK32 is the wildtype *bbk32* construct (B314/pCD100), R248A is the *bbk32*-
721 R248A isolate (B314/pAP5), K327A is the *bbk32*-K327A isolate (B314/pAP6), and R248A-
722 K327A is the *bbk32*-R248A-K327A double mutant (B314/pAP7). Numbers on the left refer to the
723 molecular mass of markers (in kDa). **C)** BBK32 mutant proteins were tested for their ability to
724 confer resistance to normal human serum (NHS). The serum sensitive strain B314 was transformed
725 separately with vector only (black), wildtype *bbk32* (blue), *bbk32* R248A (green), *bbk32* K327A
726 (purple), and *bbk32* R248A-K327A (red) and incubated with NHS. Sensitivity was scored as a
727 ratio of the affected cells relative to the total cells viewed via darkfield microscopy. Heat
728 inactivated NHS (hiNHS) was used as a control (right). P-values between *bbk32* samples are
729 indicated above. Statistical significance was assessed using a two-way ANOVA.

730

731

732

733

734

735

736

737

738

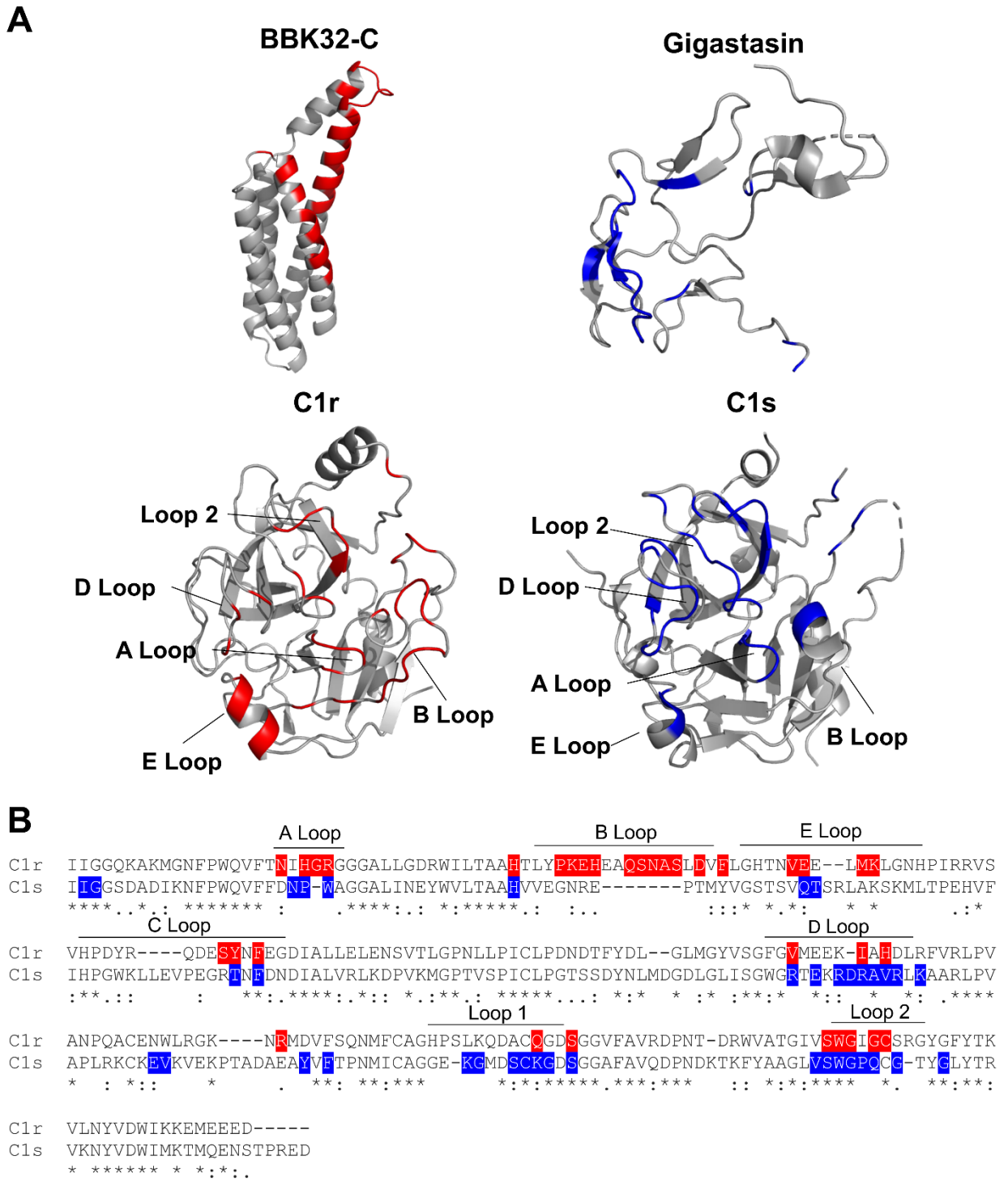

Figure 5. Comparison of BBK32 to gigastasin reveals convergent mechanisms of action. A) Ribbon diagrams of BBK32-C (PDB:6N1L), C1r-CCP2-SP (PDB:1MD8), Gigastasin/C1s-CCP2-

742 SP (PDB: 5UBM) with colored interactions within 4 Å, as judged by the program CCP4i
743 CONTACTS. The BBK32-C/C1r-CCP2-SP interactions are shown highlighted in red and
744 C1s/Gigastasin loop interactions in blue. **B)** Sequence alignment of serine protease domains of C1r
745 and C1s loops are designated with bars and are according to C1r structure.

746

747 **Table 1. MALS and SAXS parameters**

Sample	Maximal dimension D_{max} (Å)	R_g (Å)	MW_{seq} (kDa)	MW_{SAXS} (kDa)	MW_{MALS} (kDa)	SAXS model fit χ^2
BBK32-C	~75	21.3 ± 0.9	16.9	19.9 ± 1.58	~19	2.08
C1r-CCP2-SP	~80	24.0 ± 0.9	37.7	31.7 ± 1.75	~40-60	1.06
BBK32-C/ C1r-CCP2-SP Complex	~85	27.8 ± 2.2	54.6	55.6 ± 4.13	~55-65	1.24

748

References

1. N. S. Merle, S. E. Church, V. Fremeaux-Bacchi, L. T. Roumenina, Complement System Part I - Molecular Mechanisms of Activation and Regulation. *Front. Immunol.* **6**, 262 (2015).

2. N. S. Merle, R. Noe, L. Halbwachs-Mecarelli, V. Fremeaux-Bacchi, L. T. Roumenina, Complement System Part II: Role in Immunity. *Front. Immunol.* **6**, 257 (2015).

3. M. J. Walport, Complement. First of two parts. *N. Engl. J. Med.* **344**, 1058–1066 (2001).

4. M. J. Walport, Complement. Second of two parts. *N. Engl. J. Med.* **344**, 1140–1144 (2001).

5. R. J. Ziccardi, Activation of the early components of the classical complement pathway under physiologic conditions. *J. Immunol. (Baltimore, Md. 1950)*. **126**, 1769–1773 (1981).

6. U. Deniz, C. H. Stuart, de Kreuk Bart-Jan, I. K. Roman, N. de Jong Rob, J. B. Frank, S. Janine, J. K. Abraham, H. S. Thomas, W. H. I. Parren Paul, G. Piet, Structures of C1-IgG1 provide insights into how danger pattern recognition activates complement. *Science (80-.).* **359**, 794–797 (2018).

7. T. H. Sharp, A. L. Boyle, C. A. Diebolder, A. Kros, A. J. Koster, P. Gros, Insights into IgM-mediated complement activation based on in situ structures of IgM-C1-C4b. *Proc. Natl. Acad. Sci. U. S. A.* **116**, 11900–11905 (2019).

8. C. A. Diebolder, F. J. Beurskens, R. N. de Jong, R. I. Koning, K. Strumane, M. A. Lindorfer, M. Voorhorst, D. Ugurlar, S. Rosati, A. J. R. Heck, J. G. J. van de Winkel, I. A. Wilson, A. J. Koster, R. P. Taylor, E. O. Saphire, D. R. Burton, J. Schuurman, P. Gros, P. W. H. I. Parren, Complement is activated by IgG hexamers assembled at the cell surface. *Science*. **343**, 1260–1263 (2014).

9. T. R. Kjaer, S. Thiel, G. R. Andersen, Toward a structure-based comprehension of the lectin pathway of complement. *Mol. Immunol.* **56** (2013), pp. 413–422.

10. J. Dobó, A. Kocsis, P. Gál, Be on Target: Strategies of Targeting Alternative and Lectin Pathway Components in Complement-Mediated Diseases. *Front. Immunol.* **9**, 1851 (2018).

11. M. K. Pangburn, H. J. Müller-Eberhard, The alternative pathway of complement. *Springer Semin. Immunopathol.* **7**, 163–192 (1984).

12. C. Q. Schmidt, J. D. Lambris, D. Ricklin, Protection of host cells by complement regulators. *Immunol. Rev.* **274**, 152–171 (2016).

13. D. Ricklin, J. D. Lambris, Complement in immune and inflammatory disorders: pathophysiological mechanisms. *J. Immunol. (Baltimore, Md. 1950)*. **190**, 3831–3838 (2013).

14. D. Ricklin, D. C. Mastellos, E. S. Reis, J. D. Lambris, The renaissance of complement therapeutics. *Nat. Rev. Nephrol.* **14**, 26–47 (2018).

786 15. J. D. Lambris, D. Ricklin, B. V Geisbrecht, Complement evasion by human pathogens.
787 *Nat. Rev. Microbiol.* **6**, 132–142 (2008).

788 16. P. Kraiczy, Hide and Seek: How Lyme Disease Spirochetes Overcome Complement
789 Attack. *Front. Immunol.* **7**, 385 (2016).

790 17. J. T. Skare, B. L. Garcia, Complement Evasion by Lyme Disease Spirochetes. *Trends*
791 *Microbiol.* (2020), , doi:10.1016/j.tim.2020.05.004.

792 18. M. Adeolu, R. S. Gupta, A phylogenomic and molecular marker based proposal for the
793 division of the genus Borrelia into two genera: the emended genus Borrelia containing
794 only the members of the relapsing fever Borrelia, and the genus Borreliella gen. nov.
795 containing the members o. *Antonie Van Leeuwenhoek*. **105**, 1049–1072 (2014).

796 19. P. Kraiczy, J. Hellwage, C. Skerka, H. Becker, M. Kirschfink, M. M. Simon, V. Brade, P.
797 F. Zipfel, R. Wallich, Complement resistance of Borrelia burgdorferi correlates with the
798 expression of BbCRASP-1, a novel linear plasmid-encoded surface protein that interacts
799 with human factor H and FHL-1 and is unrelated to Erp proteins. *J. Biol. Chem.* **279**,
800 2421–2429 (2004).

801 20. K. Hartmann, C. Corvey, C. Skerka, M. Kirschfink, M. Karas, V. Brade, J. C. Miller, B.
802 Stevenson, R. Wallich, P. F. Zipfel, P. Kraiczy, Functional characterization of BbCRASP-
803 2, a distinct outer membrane protein of Borrelia burgdorferi that binds host complement
804 regulators factor H and FHL-1. *Mol. Microbiol.* **61**, 1220–1236 (2006).

805 21. B. Stevenson, K. Tilly, P. A. Rosa, A family of genes located on four separate 32-kilobase
806 circular plasmids in Borrelia burgdorferi B31. *J. Bacteriol.* **178**, 3508–3516 (1996).

807 22. B. Stevenson, N. El-Hage, M. A. Hines, J. C. Miller, K. Babb, Differential binding of host
808 complement inhibitor factor H by Borrelia burgdorferi Erp surface proteins: A possible
809 mechanism underlying the expansive host range of Lyme disease spirochetes. *Infect.*
810 *Immun.* (2002), doi:10.1128/IAI.70.2.491-497.2002.

811 23. J. V McDowell, J. Wolfgang, E. Tran, M. S. Metts, D. Hamilton, R. T. Marconi,
812 Comprehensive analysis of the factor h binding capabilities of borrelia species associated
813 with lyme disease: delineation of two distinct classes of factor h binding proteins. *Infect.*
814 *Immun.* **71**, 3597–3602 (2003).

815 24. J. V McDowell, K. M. Hovis, H. Zhang, E. Tran, J. Lankford, R. T. Marconi, Evidence
816 that the BBA68 protein (BbCRASP-1) of the Lyme disease spirochetes does not
817 contribute to factor H-mediated immune evasion in humans and other animals. *Infect.*
818 *Immun.* **74**, 3030–3034 (2006).

819 25. T. Bykowski, M. E. Woodman, A. E. Cooley, C. A. Brissette, R. Wallich, V. Brade, P.
820 Kraiczy, B. Stevenson, Borrelia burgdorferi complement regulator-acquiring surface
821 proteins (BbCRASPs): Expression patterns during the mammal-tick infection cycle. *Int. J.*
822 *Med. Microbiol. IJMM*. **298 Suppl**, 249–256 (2008).

823 26. M. R. Kenedy, S. R. Vuppala, C. Siegel, P. Kraiczy, D. R. Akins, CspA-mediated binding
824 of human factor H inhibits complement deposition and confers serum resistance in
825 Borrelia burgdorferi. *Infect. Immun.* **77**, 2773–2782 (2009).

826 27. E. A. Rogers, S. V Abdunnur, J. V McDowell, R. T. Marconi, Comparative analysis of the
827 properties and ligand binding characteristics of CspZ, a factor H binding protein, derived
828 from Borrelia burgdorferi isolates of human origin. *Infect. Immun.* **77**, 4396–4405 (2009).

829 28. M. R. Kenedy, D. R. Akins, The OspE-related proteins inhibit complement deposition and
830 enhance serum resistance of Borrelia burgdorferi, the lyme disease spirochete. *Infect.*
831 *Immun.* **79**, 1451–1457 (2011).

832 29. C. Hammerschmidt, Y. Klevenhaus, A. Koenigs, T. Hallström, V. Fingerle, C. Skerka, K.
833 M. Pos, P. F. Zipfel, R. Wallich, P. Kraiczy, BGA66 and BGA71 facilitate complement
834 resistance of Borrelia bavariensis by inhibiting assembly of the membrane attack complex.
835 *Mol. Microbiol.* **99**, 407–424 (2016).

836 30. T. Hallström, C. Siegel, M. Mörgelin, P. Kraiczy, C. Skerka, P. F. Zipfel, CspA from
837 Borrelia burgdorferi inhibits the terminal complement pathway. *MBio*. **4**, 13 (2013).

838 31. M. Pausa, V. Pellis, M. Cinco, P. G. Giulianini, G. Presani, S. Perticarari, R. Murgia, F.
839 Tedesco, Serum-resistant strains of Borrelia burgdorferi evade complement-mediated
840 killing by expressing a CD59-like complement inhibitory molecule. *J. Immunol.*
841 *(Baltimore, Md. 1950)*. **170**, 3214–3222 (2003).

842 32. J. A. Caine, Y.-P. Lin, J. R. Kessler, H. Sato, J. M. Leong, J. Coburn, Borrelia burgdorferi
843 outer surface protein C (OspC) binds complement component C4b and confers
844 bloodstream survival. *Cell. Microbiol.* **19** (2017), doi:10.1111/cmi.12786.

845 33. B. L. Garcia, H. Zhi, B. Wager, M. Höök, J. T. Skare, Borrelia burgdorferi BBK32
846 Inhibits the Classical Pathway by Blocking Activation of the C1 Complement Complex.
847 *PLoS Pathog.* **12**, e1005404 (2016).

848 34. M. He, B. K. Boardman, D. Yan, X. F. Yang, Regulation of expression of the fibronectin-
849 binding protein BBK32 in Borrelia burgdorferi. *J. Bacteriol.* **189**, 8377–8380 (2007).

850 35. J. Seshu, M. D. Esteve-Gassent, M. Labandeira-Rey, J. H. Kim, J. P. Trzeciakowski, M.
851 Höök, J. T. Skare, Inactivation of the fibronectin-binding adhesin gene bbk32 significantly
852 attenuates the infectivity potential of Borrelia burgdorferi. *Mol. Microbiol.* **59**, 1591–1601
853 (2006).

854 36. J. A. Hyde, E. H. Weening, M. Chang, J. P. Trzeciakowski, M. Höök, J. D. Cirillo, J. T.
855 Skare, Bioluminescent imaging of Borrelia burgdorferi in vivo demonstrates that the
856 fibronectin-binding protein BBK32 is required for optimal infectivity. *Mol. Microbiol.* **82**,
857 99–113 (2011).

858 37. W. S. Probert, J. H. Kim, M. Höök, B. J. Johnson, Mapping the ligand-binding region of
859 Borrelia burgdorferi fibronectin-binding protein BBK32. *Infect. Immun.* **69**, 4129–4133
860 (2001).

861 38. J. R. Fischer, K. T. LeBlanc, J. M. Leong, Fibronectin binding protein BBK32 of the
862 Lyme disease spirochete promotes bacterial attachment to glycosaminoglycans. *Infect.*
863 *Immun.* **74**, 435–441 (2006).

864 39. T. J. Moriarty, M. Shi, Y.-P. Lin, R. Ebady, H. Zhou, T. Odisho, P.-O. Hardy, A. Salman-
865 Dilgimen, J. Wu, E. H. Weening, J. T. Skare, P. Kubes, J. Leong, G. Chaconas, Vascular

866 binding of a pathogen under shear force through mechanistically distinct sequential
867 interactions with host macromolecules. *Mol. Microbiol.* **86**, 1116–1131 (2012).

868 40. R. Ebady, A. F. Niddam, A. E. Boczula, Y. R. Kim, N. Gupta, T. T. Tang, T. Odisho, H.
869 Zhi, C. A. Simmons, J. T. Skare, T. J. Moriarty, Biomechanics of Borrelia burgdorferi
870 Vascular Interactions. *Cell Rep.* **16**, 2593–2604 (2016).

871 41. J. Xie, H. Zhi, R. J. Garrigues, A. Keightley, B. L. Garcia, J. T. Skare, Structural
872 determination of the complement inhibitory domain of Borrelia burgdorferi BBK32
873 provides insight into classical pathway complement evasion by Lyme disease spirochetes.
874 *PLoS Pathog.* **15**, e1007659 (2019).

875 42. R. P. Rambo, J. A. Tainer, Accurate assessment of mass, models and resolution by small-
876 angle scattering. *Nature* (2013), doi:10.1038/nature12070.

877 43. M. Budayova-Spano, W. Grabarse, N. M. Thielens, H. Hillen, M. Lacroix, M. Schmidt, J.
878 C. Fontecilla-Camps, G. J. Arlaud, C. Gaboriaud, Monomeric structures of the zymogen
879 and active catalytic domain of complement protease c1r: further insights into the c1
880 activation mechanism. *Struct. (London, Engl. 1993)*. **10**, 1509–1519 (2002).

881 44. B. Webb, A. Sali, *Curr. Protoc. Bioinforma.*, in press,
882 doi:10.1002/0471250953.bi0506s47.

883 45. E. F. Pettersen, T. D. Goddard, C. C. Huang, G. S. Couch, D. M. Greenblatt, E. C. Meng,
884 T. E. Ferrin, UCSF Chimera - A visualization system for exploratory research and
885 analysis. *J. Comput. Chem.* **25**, 1605–1612 (2004).

886 46. D. Schneidman-Duhovny, M. Hammel, J. A. Tainer, A. Sali, Accurate SAXS profile
887 computation and its assessment by contrast variation experiments. *Biophys. J.* **105**, 962–
888 974 (2013).

889 47. D. Schneidman-Duhovny, M. Hammel, J. A. Tainer, A. Sali, *FoXS, FoXSDock and*
890 *MultiFoXS: Single-state and multi-state structural modeling of proteins and their*
891 *complexes based on SAXS profiles* (2016;
892 https://www.ncbi.nlm.nih.gov/pmc/articles/PMC4987932/), vol. 44.

893 48. D. Schneidman-Duhovny, M. Hammel, A. Sali, Macromolecular Docking Restrained by a
894 Small Angle X-Ray Scattering Profile (2010), doi:10.1016/j.jsb.2010.09.023.

895 49. D. Franke, D. I. Svergun, DAMMIF, a program for rapid ab-initio shape determination in
896 small-angle scattering. *J. Appl. Crystallogr.* (2009), doi:10.1107/S0021889809000338.

897 50. V. V. Volkov, D. I. Svergun, in *Journal of Applied Crystallography* (2003).

898 51. M. Pelikan, G. L. Hura, M. Hammel, Structure and flexibility within proteins as identified
899 through small angle X-ray scattering. *Gen. Physiol. Biophys.* (2009),
900 doi:10.4149/gpb_2009_02_174.

901 52. M. D. Winn, C. C. Ballard, K. D. Cowtan, E. J. Dodson, P. Emsley, P. R. Evans, R. M.
902 Keegan, E. B. Krissinel, A. G. W. Leslie, A. McCoy, S. J. McNicholas, G. N. Murshudov,
903 N. S. Pannu, E. A. Potterton, H. R. Powell, R. J. Read, A. Vagin, K. S. Wilson, Overview
904 of the CCP4 suite and current developments. *Acta Crystallogr. Sect. D Biol. Crystallogr.*

905 (2011), , doi:10.1107/S0907444910045749.

906 53. E. Krissinel, K. Henrick, Inference of Macromolecular Assemblies from Crystalline State.
907 *J. Mol. Biol.* **372**, 774–797 (2007).

908 54. R. Karlsson, P. S. Katsamba, H. Nordin, E. Pol, D. G. Myszka, Analyzing a kinetic
909 titration series using affinity biosensors. *Anal. Biochem.* **349**, 136–147 (2006).

910 55. J. Kardos, P. Gal, L. Szilagyi, N. M. Thielens, K. Szilagyi, Z. Lorincz, P. Kulcsar, L. Graf,
911 G. J. Arlaud, P. Zavodszky, The Role of the Individual Domains in the Structure and
912 Function of the Catalytic Region of a Modular Serine Protease, C1r. *J. Immunol.* **167**,
913 5202–5208 (2001).

914 56. A. Sadziene, B. Wilske, M. S. Ferdows, A. G. Barbour, The cryptic ospC gene of Borrelia
915 burgdorferi B31 is located on a circular plasmid. *Infect. Immun.* **61**, 2192–2195 (1993).

916 57. A. Sadziene, D. D. Thomas, A. G. Barbour, Borrelia burgdorferi mutant lacking Osp:
917 biological and immunological characterization. *Infect. Immun.* **63**, 1573–1580 (1995).

918 58. S. S. Pang, L. C. Wijeyewickrema, L. Hor, S. Tan, E. Lameignere, E. M. Conway, A. M.
919 Blom, F. C. Mohlin, X. Liu, R. J. Payne, J. C. Whisstock, R. N. Pike, The Structural Basis
920 for Complement Inhibition by Gigastasin, a Protease Inhibitor from the Giant Amazon
921 Leech. *J. Immunol. (Baltimore, Md. 1950)*. **199**, 3883–3891 (2017).

922 59. J. L. Schmitz, S. D. Lovrich, S. M. Callister, R. F. Schell, Depletion of complement and
923 effects on passive transfer of resistance to infection with Borrelia burgdorferi. *Infect.*
924 *Immun.* **59**, 3815–3818 (1991).

925 60. S. W. Barthold, L. K. Bockenstedt, Passive immunizing activity of sera from mice
926 infected with Borrelia burgdorferi. *Infect. Immun.* **61**, 4696–4702 (1993).

927 61. E. Fikrig, L. K. Bockenstedt, S. W. Barthold, M. Chen, H. Tao, P. A. Salaam, S. R.
928 Telford, R. A. Flavell, Sera from patients with chronic lyme disease protect mice from
929 lyme borreliosis. *J. Infect. Dis.* **169**, 568–574 (1994).

930 62. M. P. Reichhardt, S. Johnson, T. Tang, T. Morgan, N. Tebeka, N. Popitsch, J. C. Deme,
931 M. M. Jore, S. M. Lea, An inhibitor of complement C5 provides structural insights into
932 activation. *Proc. Natl. Acad. Sci. U. S. A.* (2020), doi:10.1073/pnas.1909973116.

933 63. K. Tyson, C. Elkins, H. Patterson, E. Fikrig, A. de Silva, Biochemical and functional
934 characterization of Salp20, an Ixodes scapularis tick salivary protein that inhibits the
935 complement pathway. *Insect Mol. Biol.* **16**, 469–479 (2007).

936 64. T. J. Schuijt, J. W. R. Hovius, N. D. Van Burgel, N. Ramamoorthi, E. Fikrig, A. P. Van
937 Dam, The tick salivary protein Salp15 inhibits the killing of serum-sensitive Borrelia
938 burgdorferi sensu lato isolates. *Infect. Immun.* (2008), doi:10.1128/IAI.00232-08.

939 65. N. C. S. Silva, V. F. Vale, P. F. Franco, N. F. Gontijo, J. G. Valenzuela, M. H. Pereira, M.
940 R. V. Sant'Anna, D. S. Rodrigues, W. S. Lima, B. Fux, R. N. Araujo, Saliva of
941 Rhipicephalus (Boophilus) microplus (Acari: Ixodidae) inhibits classical and alternative
942 complement pathways. *Parasites and Vectors* (2016), doi:10.1186/s13071-016-1726-8.

943 66. T. J. Schuijt, J. Coumou, S. Narasimhan, J. Dai, K. Deponte, D. Wouters, M. Brouwer, A.
944 Oei, J. J. T. H. Roelofs, A. P. van Dam, T. van der Poll, C. V. Veer, J. W. Hovius, E.
945 Fikrig, A tick mannose-binding lectin inhibitor interferes with the vertebrate complement
946 cascade to enhance transmission of the lyme disease agent. *Cell Host Microbe*. **10**, 136–
947 146 (2011).

948 67. V. P. Ferreira, V. Fazito Vale, M. K. Pangburn, M. Abdeladhim, A. Ferreira Mendes-
949 Sousa, I. V. Coutinho-Abreu, M. Rasouli, E. A. Brandt, C. Meneses, K. F. Lima, R.
950 Nascimento Araújo, M. Horácio Pereira, M. Kotsyfakis, F. Oliveira, S. Kamhawi, J. M. C.
951 Ribeiro, N. F. Gontijo, N. Collin, J. G. Valenzuela, SALO, a novel classical pathway
952 complement inhibitor from saliva of the sand fly Lutzomyia longipalpis. *Sci. Rep.* (2016),
953 doi:10.1038/srep19300.

954 68. A. F. Mendes-Sousa, D. C. Queiroz, V. F. Vale, J. M. C. Ribeiro, J. G. Valenzuela, N. F.
955 Gontijo, J. F. Andersen, An Inhibitor of the Alternative Pathway of Complement in Saliva
956 of New World Anopheline Mosquitoes. *J. Immunol.* (2016),
957 doi:10.4049/jimmunol.1600020.

958 69. B. L. Garcia, K. X. Ramyar, D. Ricklin, J. D. Lambris, B. V Geisbrecht, Advances in
959 understanding the structure, function, and mechanism of the SCIN and Efb families of
960 Staphylococcal immune evasion proteins. *Adv. Exp. Med. Biol.* **946**, 113 (2012).

961 70. B. L. Garcia, S. A. Zwarthoff, S. H. M. Rooijakkers, B. V Geisbrecht, Novel Evasion
962 Mechanisms of the Classical Complement Pathway. *J. Immunol.* **197**, 2051–2060 (2016).

963 71. C. Dunwiddie, N. A. Thornberry, H. G. Bull, M. Sardana, P. A. Friedman, J. W. Jacobs,
964 E. Simpson, Antistasin, a leech-derived inhibitor of factor Xa. Kinetic analysis of enzyme
965 inhibition and identification of the reactive site. *J. Biol. Chem.* **264**, 16694–16699 (1989).

966 72. P. Kraiczy, Travelling between Two Worlds: Complement as a Gatekeeper for an
967 Expanded Host Range of Lyme Disease Spirochetes. *Vet. Sci.* **3** (2016),
968 doi:10.3390/vetsci3020012.

969 73. D. S. Samuels, D. Drecktrah, L. S. Hall, Genetic Transformation and Complementation.
970 *Methods Mol. Biol.* **1690**, 183–200 (2018).

971 74. J. A. Hyde, E. H. Weening, J. T. Skare, Genetic transformation of Borrelia burgdorferi.
972 *Curr. Protoc. Microbiol.* **Chapter 12** (2011), doi:10.1002/9780471729259.mc12c04s20.

973 75. B. V Geisbrecht, S. Bouyain, M. Pop, An optimized system for expression and
974 purification of secreted bacterial proteins. *Protein Expr. Purif.* **46**, 23–32 (2006).

975 76. B. R. Rushing, D. L. Rohlik, S. Roy, D. A. Skaff, B. L. Garcia, Targeting the Initiator
976 Protease of the Classical Pathway of Complement Using Fragment-Based Drug
977 Discovery. *Molecules* (2020), doi:10.3390/molecules25174016.

978 77. K. N. Dyer, M. Hammel, R. P. Rambo, S. E. Tsutakawa, I. Rodic, S. Classen, J. A. Tainer,
979 G. L. Hura, High-throughput SAXS for the characterization of biomolecules in solution: A
980 practical approach. *Methods Mol. Biol.* (2014), doi:10.1007/978-1-62703-691-7_18.

981 78. G. L. Hura, A. L. Menon, M. Hammel, R. P. Rambo, F. L. Poole, S. E. Tsutakawa, F. E.
982 Jenney, S. Classen, K. A. Frankel, R. C. Hopkins, S. J. Yang, J. W. Scott, B. D. Dillard,

M. W. W. Adams, J. A. Tainer, Robust, high-throughput solution structural analyses by small angle X-ray scattering (SAXS). *Nat. Methods* (2009), doi:10.1038/nmeth.1353.

79. P. V. Konarev, V. V. Volkov, A. V. Sokolova, M. H. J. Koch, D. I. Svergun, PRIMUS: A Windows PC-based system for small-angle scattering data analysis. *J. Appl. Crystallogr.* (2003), doi:10.1107/S0021889803012779.

80. D. I. Svergun, Determination of the regularization parameter in indirect-transform methods using perceptual criteria. *J. Appl. Crystallogr.* (1992), doi:10.1107/S0021889892001663.

81. P. Emsley, B. Lohkamp, W. G. Scott, K. Cowtan, Features and development of Coot. *Acta Crystallogr. D. Biol. Crystallogr.* **66**, 486–501 (2010).

82. G. Q. Dong, H. Fan, D. Schneidman-Duhovny, B. Webb, A. Sali, Structural bioinformatics Optimized atomic statistical potentials: assessment of protein interfaces and loops. **29**, 3158–3166 (2013).

83. K. Manalastas-Cantos, P. V. Konarev, N. R. Hajizadeh, A. G. Kikhney, M. V. Petoukhov, D. S. Molodenskiy, A. Panjkovich, H. D. T. Mertens, A. Gruzinov, C. Borges, C. M. Jeffries, D. I. Svergun, D. Franke, ATSAS 3.0 : expanded functionality and new tools for small-angle scattering data analysis . *J. Appl. Crystallogr.* (2021), doi:10.1107/s1600576720013412.

84. Z. Otwinowski, W. Minor, (Academic Press, 1997; http://www.sciencedirect.com/science/article/pii/S007668799776066X), vol. 276 of *Methods in Enzymology*, pp. 307–326.

85. P. D. Adams, P. V Afonine, G. Bunkóczi, V. B. Chen, I. W. Davis, N. Echols, J. J. Headd, L.-W. Hung, G. J. Kapral, R. W. Grosse-Kunstleve, A. J. McCoy, N. W. Moriarty, R. Oeffner, R. J. Read, D. C. Richardson, J. S. Richardson, T. C. Terwilliger, P. H. Zwart, PHENIX: a comprehensive Python-based system for macromolecular structure solution. *Acta Crystallogr. D. Biol. Crystallogr.* **66**, 213–221 (2010).

86. J. Kardos, V. Harmat, A. Palló, O. Barabás, K. Szilágyi, L. Gráf, G. Náray-Szabó, Y. Goto, P. Závodszky, P. Gál, Revisiting the mechanism of the autoactivation of the complement protease C1r in the C1 complex: Structure of the active catalytic region of C1r. *Mol. Immunol.* **45**, 1752–1760 (2008).

87. A. Roos, L. H. Bouwman, J. Munoz, T. Zuiverloon, M. C. Faber-Krol, F. C. den Houten, N. Klar-Mohamad, C. E. Hack, M. G. Tilanus, M. R. Daha, Functional characterization of the lectin pathway of complement in human serum. *Mol. Immunol.* **39**, 655–668 (2003).

88. I. Schechter, A. Berger, On the size of the active site in proteases. I. Papain. *Biochem. Biophys. Res. Commun.* (1967), doi:10.1016/S0006-291X(67)80055-X.